Mechanochemical activation of nickel oxide: a pivotal step in the process chain enabling binder-free-anodes for alkaline water electrolysis

Mohit Chatwani[1], Adarsh Jain[1], Christian Marcks[2], Jacob Johny[4], Lars Grebener[1], Hao Yun[1], Ali Raza Khan[4], Georg Bendt[5], Stefan Romeis[6], Viktor Čolić[3,4], Marc Frederic Tesch[4], Anna K. Mechler[2], Vineetha Vinayakumar[1,3], Doris Segets* [1,3]

1. Institute for Energy and Materials Processes–Particle Science and Technology (EMPI–PST), University of Duisburg-Essen (UDE), Duisburg, Germany;
2. Electrochemical Reaction Engineering (AVT.ERT), RWTH Aachen University, Aachen, Germany;
3. Center for Nanointegration Duisburg-Essen (CENIDE), University of Duisburg-Essen (UDE), Duisburg, Germany;
4. Max Planck Institute for Chemical Energy Conversion (MPI-CEC), Mülheim an der Ruhr, Germany
5. Faculty of Chemistry, University of Duisburg-Essen (UDE), Essen, Germany
6. Siegwerk Druckfarben AG & Co. Kgaa

Email: doris.segets@uni-due.de

Sustainable hydrogen production via alkaline water electrolysis (AWE) demands robust electrocatalysts for the oxygen evolution reaction (OER) that combine performance with scalability. Herein, we address critical challenges in AWE by mechanochemical activation of nickel oxide (NiO), enabling the fabrication of binder-free anodes. First, we investigated the effects of planetary ball milling on NiO, which include a decrease in crystallite size, increase in specific surface area, elevated Ni^{3+} content, and enhanced surface hydroxyl concentration. Milling with larger beads induced more pronounced structural transformations due to higher impact forces. Electrochemical testing revealed an improved overpotential of the mechanochemically activated NiO compared to the bare Ni plate substrate (365 mV vs. 377 mV at 100 mA cm^{-2} in 1 M KOH), with excellent particle-particle cohesion enabling mechanically stable, binder-free anodes. Post-OER analysis using X-ray photoelectron spectroscopy identified hydroxyl-mediated cohesion and adhesion as key factors for mechanical integrity and performance. Building on these insights, we translated the approach to scalable stirred media milling, which enables direct ink formulation. Milling in isopropanol suppressed reagglomeration and eliminated the need for an intermediate drying step. The resulting NiO exhibited even lower overpotential (343 mV) and high mechanical robustness, offering a streamlined, binder-free strategy for OER electrode fabrication.

1. Introduction

The escalating global imperative for sustainable and clean energy solutions has amplified the pursuit of efficient energy storage mechanisms. Hydrogen emerges as a superior energy vector, attributed to its high gravimetric energy density and environmental generosity[1]. AWE is an important method for hydrogen production, relying on the OER to generate oxygen and electrons at the anode. OER, involving a complex four-electron transfer process, significantly impacts the overall efficiency of AWE due to its sluggish kinetics and high overpotentials caused by the noticeable energy barrier[2]. This highlights the importance of developing efficient electrocatalysts, thereby improving the viability of hydrogen as a clean energy source[3,4]. Noble metal-based catalysts such as iridium oxide (IrO_2) and ruthenium oxide (RuO_2) are among the most efficient OER electrocatalysts, owing to their high electrocatalytic activity in both alkaline and acidic media[5,6]. Despite their remarkable performance, the extensive deployment of IrO_2 and RuO_2 in OER applications is severely constrained by their exorbitant costs and the limited availability of iridium and ruthenium[7,8]. Consequently, current research endeavors are increasingly focusing on non-noble metal alternatives, particularly those incorporating 3d transition metals, which demonstrate catalytic properties analogous to their noble metal counterparts[9].

A diverse array of non-noble-metal-based electrocatalysts has been found and synthesized so far, encompassing metals and alloys[10,11], oxides[12], hydroxides[13,14], chalcogenides[15], borides[16], and other related compounds. Among these, metal oxides have garnered significant attention due to their unique electronic structures, abundant availability, and tunable catalytic properties. These materials offer a cost-effective alternative and at the same time exhibit exceptional stability and durability under operational conditions[17]. In particular, NiO has emerged as a promising candidate for alkaline OER[18]. Its chemical stability, reasonable electrical conductivity, durability under operational conditions, and excellent catalytic performance make it a suitable material for large-scale AWE applications at industrial operation conditions[19]. Though alternatives are emerging, anodes for AWE are typically prepared by formulating catalytic powders into inks, which are then coated onto substrates.

However, larger-sized powders often exhibit limitations such as poor ink stability caused by fast sedimentation[20]. This sedimentation challenge persists even with optimized ink formulations as large particles are inevitably governed by gravity. Beyond particle size, another significant challenge is the large-scale availability of efficient materials. On the one hand, high-performance materials are often developed in research projects at the lab scale, but, because of a lack of process technology for nanomaterials[21], their production is rarely scalable to reasonable amounts of at least several grams, ideally kilograms. These amounts are however needed for large-area coatings and subsequent electrode integration into electrolysers to enable the execution of parameter studies needed for scale-up. On the other hand, commercially available materials, while readily available, often exhibit lower catalytic activity, are not available on the nanoscale, and require higher overpotentials for OER. These combined limitations highlight the critical need for the scalable preparation of active anode materials that enable the required research and understanding to bridge the gap between laboratory research and practical applications.

Another challenge relates to the use of binders in anode preparation. Binders, such as ionomers or polymeric adhesives, are traditionally incorporated into electrocatalyst ink formulations to ensure mechanical stability of the anode after drying. In brief, mechanical stability refers to the interplay of adhesion between the catalyst particles and the substrate, and particle-particle-cohesion. These particle-substrate and particle-particle contacts are also

crucial for the formation of conductive networks that facilitate efficient electron and ion transport during the OER process[22]. While binders are commonly added to inks to provide anode layers of high mechanical cohesion and adhesion, their inclusion also introduces certain limitations which must be addressed to ensure optimal anode performance[23]. First, this reliance on binders, such as quaternary ammonium-based binders[24], poses economic and regulatory challenges due to their toxicity and high production cost. Second, the presence of a binder increases the complexity of the ink formulation. Third, it impedes the overall conductivity of the catalyst layer, thereby contributing to ohmic resistance (i.e., losses arising from electron transport limitations across poorly conductive binder domains)[23]. Finally, binders can potentially degrade under harsh electrochemical conditions which can lead to diminished long-term performance[25]. Altogether, these challenges have sparked interest in exploring strategies for preparing binder-free anodes for OER[26]. A notable example to achieve binder-free anodes includes the work by Hemmati et al., who succeeded in fabricating an anode that consisted of a binder-free catalyst layer of NiO nanorods deposited on a Ni foam. These nanorod arrays were prepared with a two-step procedure of hydrothermal and annealing processes, and then used as porous transport layer which resulted in an overpotential of 350 mV at 100 mA cm^{-2} in 1 M KOH[27]. However, despite the significant advancements in binder-free anodes, the scalability and industrial viability of these methods remain a major concern, necessitating innovative fabrication strategies that ensure process reliability, material stability, and enhanced catalytic performance.

To address these limitations, few researchers, such as Bhandari et al., have demonstrated that planetary ball milling Co- and Ni-based oxides can yield significant performance enhancements[28]. In their work, fluorine-containing Nafion was used as the binder that was added to the catalyst ink formulation to form stable anodes. Through a combination of hydrothermal synthesis and subsequent ball milling, $NiCoO_2$ was demonstrated to achieve an overpotential of 330 mV at 10 mA cm^{-2} in 1 M KOH which highlights the potential of planetary ball milling in tailoring material properties for improved electrochemical performance. Similarly, Kahimbi et al. utilized ball milling to process bulk Ni and graphite oxide for supercapacitor applications, achieving high specific capacitance and superior cycling stability due to the increased surface area and improved porosity[29]. However**,** while mechanochemical activation has been studied to enhance surface activation and reduce particle size, its potential for developing binder-free anodes for OER remains largely unexplored. This presents a significant challenge for the scalable development of high-performance, binder-free electrode materials suitable for industrial AWE systems.

In this study, we employ a wide range of impact forces and specific energy inputs using ball milling and stirred media milling to investigate how a controlled mechanical energy input transforms the physicochemical properties of pristine NiO. These include particle morphology, crystallite size, specific surface area, Ni^{3+} content, oxygen vacancies, and surface hydroxylation. In the first step, targeting a general understanding, powders from planetary ball milling were formulated into binder-free, sedimentation-stable inks and spray-deposited onto Ni substrates. The resulting anodes exhibited excellent mechanical stability and robust electrochemical performance for the NiO material, with an overpotential of 365 mV at 100 mA cm^{-2} including no delamination. Through comprehensive characterization of microstructural and macroscopic layer properties, we accounted hydroxyl-mediated particle-particle cohesion for the pronounced mechanical integrity of these binder-free electrodes. In the second step, we exploit this understanding and demonstrate relevance. The strategy was extended to stirred media milling—a scalable wet grinding process performed in liquid phase—which effectively suppressed reagglomeration and eliminated the need for powder isolation, drying, and

redispersion upon mechanochemical activation. The resulting electrodes demonstrated a further reduction in overpotential to 343 mV at 100 mA cm^{-2} along with enhanced structural stability. These improvements arise from a synergistic interplay of enhanced hydroxylation, improved particle-particle cohesion, increased wettability, and strengthened mechanical adhesion—all of which collectively contribute to the superior electrochemical and structural performance of the resulting electrodes. We believe that the method of stirred media milling holds substantial promise for the scalable preparation of active, binder-free anodes for AWE.

2. Experimental section

2.1 Materials and chemicals

NiO (Sigma-Aldrich, 99.995 %), Yttrium stabilized zirconium oxide (ZrO_2) beads (Retsch, 0.3 mm and 2.5 mm), milli-Q water (resistivity >18.1 MΩ·cm), absolute ethanol (EtOH, VWR International, 99.97 %), dimethylformamide (DMF, VWR Chemicals, 99.9 %), dimethyl sulfoxide (DMSO, Sigma-Aldrich, >99.9 %), tetrahydrofuran (THF, VWR Chemicals, 100 %), IPA (VWR International, 99.99 %), propylene carbonate (PC, Sigma-Aldrich, 99 %), nickel metal plates (HMW Hauner, Ra <0.1, 99.2 %, projected area 1 cm^2), and potassium hydroxide (KOH) pellets (Sigma-Aldrich, 85 %) were used as received.

2.2 Planetary ball milling and stirred media milling

For all planetary ball milling experiments, a planetary ball mill (Retsch PM-100) was used. A total of 312.5 mg of commercial nickel oxide (NiO) powder was mixed with 46.9 g of yttria-stabilized zirconia (YSZ) beads, maintaining a fixed powder-to-beads mass ratio of 1:150. Additionally, 2 µL mg^{-1} milli-Q water (relative to the catalyst powder) was added to a 50 mL zirconia milling jar. The rotational speed was set to 400 rpm, with a total milling duration of 2 hours. To manage thermal effects, a cooling interval of 1 minute was introduced between the milling cycles. During operation, a maximum temperature of approximately 50 °C was recorded at the outlet. The rotational direction was alternated between clockwise and anticlockwise every 30 minutes to ensure uniform mixing and grinding.

The ball milling process utilized two different bead sizes, 0.3 mm (higher specific energy input[30], labelled as P-0.3) and 2.5 mm (lower specific energy input, labelled as P-2.5). Following the milling process, the resulting material was flushed out the milling jar using milli-Q water. It was then subsequently dried in a vacuum oven at 60 °C for 20 hours to ensure complete removal of residual moisture.

For the exploitation study, liquid-phase stirred media milling was applied using a Bühler PML2 MML. The experiment was performed using 0.3 mm YSZ as milling beads, with NiO solid content of 6.6 % in IPA as the continuous phase. A 70 mL silicon carbide milling jar was used, filled to 85 % of its volume with beads and the feed material. The mill was operated at a tip speed of 12.1 m s^{-1} and a throughput of 36 kg/h in recirculation mode, with a gross power input of 0.8 kW. The process was conducted up to a specific energy of 2.45 kWh kg^{-1} relative to the suspension, corresponding to a total processing time of 106 minutes. For cooling, propylene glycol was used, and sealing was applied to prevent excessive heat buildup and evaporation of IPA. The outlet temperature during processing was maintained at approximately 27 °C. Following milling, the resulting suspension was diluted with IPA to a final concentration of ~0.13 wt% (equivalent to 1 mg mL^{-1}) for further characterization and electrode fabrication.

2.3 Ink formulation and layer deposition

2.3.1 Dispersion and ink preparation, and their characterization

Both, dispersions for analysis of Hansen solubility parameters (HSP) and catalyst inks for the coating of anode layers were prepared with a solid concentration of 1 mg mL^{-1}. For HSP determination, the catalyst powder was dispersed in selected probe liquids[31] (EtOH, IPA, DMF, DMSO, NMP, PC, and THF). For catalyst particle dispersion, a tip Sonicator (Branson SFX550) was used at an amplitude of 40 % for 6 min. An ice bath was employed to prevent overheating.

Characterization was performed by utilizing an analytical centrifuge (LUMisizer 6514–44, LUM GmbH). Samples of 410 µL were filled into polyamide cells (used for DMF, DMSO, NMP, PC, and THF) and polycarbonate cells (used for ethanol and IPA) and placed inside the centrifuge. All measurements were conducted at 1500 RPM and 20 °C. The captured fingerprints were then visualized by transmittograms that enable improved understanding of the sedimentation dynamics and direct comparison of dispersions and inks[32].

2.3.2 Spray coating

Ni plates were used as a support for the fabrication of all anodes. Before coating, the nickel plates were cleaned with water, 1 M HCl solution, acetone, and IPA in a sonication bath (Elmasonic S 30 H, Germany) at room temperature (RT) for 5 min each.

The catalyst deposition was conducted using an ultrasonic spray coater (Sono Tek Co., NY). After preparation of the anode support, the as-prepared catalyst ink was pumped from the liquid delivery system of the spray coater to the spray-forming tip. In brief, due to the ultrasonic energy input, the ink breaks up into small droplets. These ink droplets distribute on the surface of the nickel support that was pre-heated to 150 °C[33]. To ensure uniform coverage, the coating was performed along two axes on the Ni plate, with a 5-second interval between each spray cycle. The flow rate of the catalyst ink was maintained at 0.4 mL min^{-1}. The final mass loading of the catalyst was measured using a precision balance (A&D BM-22 microbalance) as approximately 250 ± 23 µg cm^{-2}, based on the difference between the initial weight of the Ni substrate and the final weight after the spray coating.

2.4 Morphological studies of powders and layers

2.4.1 Transmission electron microscopy

Transmission electron microscopy (TEM) measurements were carried out on a Jeol JEM 2200 fs microscope (Akishima, Japan) equipped with a probe-side Cs corrector operated at 200 kV acceleration voltage. The powder material was suspended in an organic solvent and then drop-casted on a carbon-coated Cu grid under ambient conditions. The images were taken in conventional bright field mode. Energy-dispersive X-ray (EDX) spectroscopy elemental mappings were acquired with an X-Max 100 detector (Oxford Instruments, Abingdon, United Kingdom). The average particle size in each case was determined by analyzing the particle diameter using ImageJ (software version 1.53e). The particle size distribution was calculated using the probability density function labelled as number density (q_0) with the units of nm^{-1} based on measurements of at least 50 particles for the NiO feed (due to a smaller number of individual particles) and 300 particles for the P-0.3 and P-2.5 samples each.

2.4.2 Optical profilometry

A non-contact 3D optical profilometer (Sensofar S Neox) based on white light interferometry (WLI) was employed. Surface scans were carried out over a representative area of 300 × 300 µm², 800 × 800 µm², and 1600 × 1600 µm², with a vertical resolution on the nanometer

scale and a lateral resolution determined by the objective lens used (10x to 50x magnification). Multiple regions on each sample (n = 5) were analyzed to ensure statistical reproducibility and representativity of the data. The acquired interferometric images were processed using the instrument's proprietary software (SensoMAP v10) for surface reconstruction and quantitative analysis of the root mean square height.

2.4.3 Scanning electron microscopy and energy-dispersive X-ray spectroscopy

Scanning electron microscopy (SEM) and EDX measurements were conducted using a Quanta 3D FEG scanning electron microscope (FEI) to analyze the morphology of powder materials. For all measurements, the device was operated along with EDX using an acceleration voltage of 30 kV to also determine the elemental composition.

2.4.4 Atomic force microscopy

The surface of spray-coated anodes was examined using an atomic force microscope (AFM, TOSCA 400, Anton Paar Germany GmbH, Germany), which allows for the measurement of surface topography with atomic-scale resolution, i.e., 0.5 nm. A commercially available silicon tip was utilized, and the microscope was operated in 'Tapping mode', where the cantilever tip intermittently contacts and taps the sample surface.

2.4.5 Nitrogen sorption measurements

Nitrogen (N_2) sorption measurements were performed to evaluate the surface area of the powder material using a volumetric adsorption analyzer (NovaStation A, Quantachrome) at 77 K. Prior to the measurements, the samples (approximately 300 mg each) were degassed under vacuum, heated to 250.0 °C at 5.0 °C min^{-1}, and then held for 960 min to remove any adsorbed impurities and moisture. The specific surface area was determined analyzing N_2 sorption data using the Brunauer–Emmett–Teller (BET) method over a relative pressure range from 0.04-0.95[34].

2.5 Chemical and structural characterization

2.5.1 Fourier Transform Infrared spectroscopy

Fourier Transform Infrared (FTIR) spectroscopy was conducted to investigate the functional groups and chemical bonding in the anode materials using a FTIR spectrometer (Bruker, Vertex 80). The instrument was equipped with a RT-DLaTGS (Room Temperature Deuterated L-Alanine doped TriGlycine Sulphate) detector and a KBr beam splitter. The transmittance spectra were recorded in attenuated total reflectance (ATR) mode over the range of 4000–200 cm^{-1} with a spectral resolution of 4 cm^{-1}.

The measurements were conducted at RT under N_2 atmosphere to prevent moisture and CO_2 interference. Each spectrum was obtained by averaging 32 scans on three different spots for each sample to improve the signal-to-noise ratio and reproducibility. The obtained spectra were then subjected to baseline correction and normalization using Bruker OPUS 9.0 to enhance the clarity and accuracy of the peaks.

2.5.2 Powder X-ray diffraction

Powder X-ray diffraction (PXRD) patterns were recorded on a Bruker D8 Advance powder diffractometer in Bragg-Brentano geometry at RT (50 mg for each sample) in the range of 2Θ = 5-90° with a step size of 0.01° using Cu Kα radiation (λ = 1.5418 Å, 40 kV, and 40 mA).

The crystallite size was estimated using the Debye Scherrer equation[35]:

$$D = \frac{K\lambda}{\beta cos\theta}$$ Equation (1)

Where D is the crystallite size, K is the shape factor (usually taken to be unity), λ is the wavelength of the X-ray radiation (1.5406 Å for Cu Kα), β is the full width at half maximum (FWHM) of the diffraction peak (in radians), and θ is the Bragg angle (in degrees).

The inter planar distance was calculated using Bragg's Law[36]:

$$n\lambda = 2dsin\theta$$ Equation (2)

The crystallinity index (CI) was determined using the maximum and minimum intensity[37]:

$$CI = \frac{I_{max} - I_{min}}{I_{max}}$$ Equation (3)

Where I_{max} is the intensity of the crystalline peak with the highest intensity. I_{min} is the intensity of the crystalline peak with the lowest intensity.

The lattice micro strain (ε) was calculated by the Williamson-Hall method[38]:

$$\varepsilon = \frac{\beta}{4tan\theta}$$ Equation (4)

2.5.3 X-ray photoelectron spectroscopy

X-ray photoelectron spectroscopy (XPS) measurements of the powders were performed using a VersaProbe II (ULVAC-Phi 5000) with a monochromatic Al Kα source. Reported sensitivity factors were corrected for the specific transmission of the instrument by a transmission function, which was calculated by measuring the different Cu peaks on a sputter-cleaned Cu foil, deriving thus machine-specific sensitivity factors. The software used for fitting was CasaXPS.

XPS analysis of the coated layers (pre- and post-OER) were performed under ultra-high vacuum (~10-8 mbar) employing XPS (SPECS GmbH) having an Al-Kα source with monochromated X-rays of energy 1486.6 eV. All the recorded spectra were calibrated using C1s at 284.8 eV. The data analysis was performed using the CasaXPS software and the peak deconvolutions were done applying a Shirley-type background.

2.5.4 Raman spectroscopy

Raman analyses of the nano-powders after ball milling were conducted using a DXR Raman microscope from Thermo Scientific. The excitation wavelength was 532 nm, and a laser power of 3 mW was employed to collect the Raman spectra.

2.5.5 Hansen solubility parameters

The HSP were determined using the two-step strategy developed by Amin et al.[31]. In the first step, EtOH, DMF, and THF were selected to determine which groups of liquids could effectively disperse the nano-powders. Based on the dispersion stability observed in this first step, additional probe liquids were then investigated. The expanded set of probe liquids ultimately informed the ranking procedure for HSP determination, following the approach described by Süß et al.[39] and refined by Bapat et al[40].

2.5.6 Zeta potential

To determine the pH-dependent Zeta-potential, we utilized the Stabino device equipped with a potentiometric titrator (Particle Metrix, Germany). Prior to each measurement, the sample was dispersed in deionized water to ensure minimal interference from extraneous ions. The resulting data is automatically converted to zeta potential values through the Smoluchowski equation[41]. Each measurement was performed in triplicate to ensure accuracy and reproducibility.

2.6 Wettability and adhesion analysis

2.6.1 Contact angle measurements

Contact angle measurements were performed using OCA15PRO equipment (Data Physics Instruments GmbH). The measurements were conducted with 1 M KOH as the liquid which was dropped on the sample surface at a dosing rate of 5 µL s^{-1}. Each measurement was performed in triplicate to ensure reproducibility.

2.6.2 Adhesion analysis

To measure the adhesion strength of the different coatings, an adhesion analyzer (LUMiFrac centrifuge, LUM GmbH) was used. This device applies centrifugal forces to a coating by the help of a copper test mass. Of particular importance is the preparation of the Ni plates that was executed as follows. A stainless steel backplate was cleaned manually with IPA and the Ni plate was placed on top of the backplate, held in place by a stripe of a double-sided PET adhesive tape with an acrylic liner (Lohmann DuploCOLL 362.2). The catalyst layer on each Ni plate was facing upwards. A round adapter (stainless steel, 7 mm diameter) was cleaned with IPA and glued on top of the catalyst layer. The copper test mass was then placed onto the adapter, so that the Ni plate with the catalyst layer was in between the backplate and the copper mass. This assembly was placed for 24 h in fasteners, so the pressure-sensitive adhesive can build up sufficient contact. Finally, the assembly was put in an aluminum guiding sleeve which ensures that all forces are applied perpendicularly, and all together into the detector on the centrifugal plate. This detector determines at which frequency the copper test mass with the adapter breaks off from the catalyst layer and the adherence can be calculated from this maximum centrifugal force and the adapter diameter. Three specimens per set of catalyst layer variations were prepared.

2.7 Electrochemical characterization

2.7.1 Rotating disk electrode measurements

Drop-casting was employed to prepare films on a clean, glassy carbon (GC) rotating disk electrode (RDE, Pine Instrument, USA) tip by pipetting four times 10 µL of NiO catalyst dispersion on the GC. The electrode was dried under N_2 gas at 150 rpm for 20 min. Prior to catalyst loading, the cleanliness of the GC electrode was confirmed by cyclic voltammetry (CV).

Electrochemical characterization was conducted in a three-electrode single-compartment cell using an RDE. A graphite rod was the counter electrode, and a reversible hydrogen electrode (HydroFlex, Germany) was used as the reference electrode. All experiments were performed at RT in 100 mL of Ar-saturated 1 M KOH (TH Geyer), with $Fe(NO_3)_3$ (Agilent, diluted in HNO_3) added to maintain a controlled iron concentration of 200 ppb in each batch. The rotation speed was kept at 1600 rpm. A Biologic potentiostat (BioLogic, France) was used to control the potential, and a modulated speed rotator (Pine Research Instrument, USA) was used to control the rotation speed. Prior to each measurement, a CV with a Pt polycrystalline electrode was recorded to confirm system cleanliness and verify the reference electrode potential.

The measurement sequence began by recording the open circuit potential (OCP) for 60 seconds to enable the system to reach a stable equilibrium potential. Potentiostatic electrochemical impedance spectroscopy (PEIS) was then performed at OCP over a frequency range of 30 kHz to 1 Hz to determine the uncompensated resistance (R_u) and apply IR correction. Before evaluating the OER, the catalyst underwent electrochemical preconditioning by cycling 50 CVs between 0.5 and 1.5 V vs. RHE at a scan rate of 100 mV s^{-1} under continuous rotation (1600 rpm). This step was essential for stabilizing the catalyst surface and eliminating residual impurities.

Subsequently, the OER activity was assessed using linear sweep voltammetry (LSV) at a scan rate of 5 mV s^{-1} with a rotation speed of 1600 rpm. Finally, the long-term stability of the catalyst was evaluated by chronopotentiometry (CP) at 10 mA cm^{-2} for one hour under identical RDE conditions.

2.7.2 Beaker cell measurements

The fabricated layers were employed as working electrodes in a three-electrode beaker cell setup. The used setup is a modified version of the cell presented by Thissen et al., which also makes it applicable for plate electrodes[42]. For this, an in-house 3D printed polymer holder with an inserted 0.5 mm Ni rod (99.5 % trace metal base, HMW Hauner) was employed as a current collector for the working and counter electrode. Mercury/mercury oxide (Hg/HgO, ALS Japan) and a fine mesh (De Nora) were employed as reference and counter electrodes, respectively. The potential of the former was regularly tracked vs. a true RHE[43]. 200 ml of 1 M KOH (TH Geyer) was employed as electrolyte, whereas iron (diluted in HNO_3, Agilent) was added to reach a controlled concentration of 200 ppb for every batch. No stirring was applied during the measurements. Gamry Interfaces 1010E and Ref3000 were used as potentiostats/galvanostats with Gamry Framework Data Acquisition Software Version 7 to control the electrochemical measurements. The electrochemical protocol was applied for every sample (triple determination), consisting of four main steps as discussed in detail below.

The protocol starts with the conditioning of the electrodes by cycling the potential 50 times from 0.2-1.45 V vs. RHE, with a scan rate of 100 mV s^{-1}. Next, the initial dynamic activity of the samples is determined by cycling the potential between 1-1.8 V vs. RHE three times, with a scan rate of 5 mV s^{-1} (“Activity 1”). The activity step is followed by a CP at 100 mA cm^{-2} for two hours. The final dynamic activity (“Activity 2”) is then determined with the same settings as for Activity 1. Before every protocol step, the R_u was determined via PEIS at open circuit potential (AC voltage 10 mV rms, 300000 Hz-1000 Hz, 10 points per decade). The R_u was determined at the lowest absolute difference from the PEIS-phase from zero. All measured potential values were corrected using their respective R_u values. For the correction of the CP, the resulting R_u of the PEIS from immediately before the CP and before the second activity measurement is arithmetically averaged, since a gradual change in the resistances during the CP was observed.

3. Results and discussion

3.1 Strategy

Figure 1 illustrates the electrode fabrication strategy. Initially, the commercial NiO was used to prepare anodes, however, its relatively large particle size hindered the formation of a sedimentation-stable ink. This instability was confirmed by sedimentation tests[32] conducted with various aqueous and organic solvents using AC (see supplementary information). In all cases, the NiO particles settled rapidly. This is ascribed primarily to the large particle size of the commercial NiO. Additionally, some degree of agglomeration or the presence of weak solid

bridges between particles which appear resistant to disruption under ultrasonic dispersion, cannot be excluded. From our experience, this is a frequently observed phenomenon with commercially available electrocatalysts, impeding scale-up-research.

To mitigate this and elevate the powder-based approach by binder-free anodes, we structured our study as follows: Two samples were prepared via planetary ball milling under varying stress intensity, achieved by altering the size of the milling beads while keeping all other parameters constant (see Experimental Section).

Following the milling process, comprehensive physicochemical characterization was performed to evaluate structural and morphological changes, with particular attention to defect-related features. Subsequently, ink formulations were developed and anodes were prepared by coating of the inks on a Ni support, accompanied by electrochemical testing and post-OER analysis.

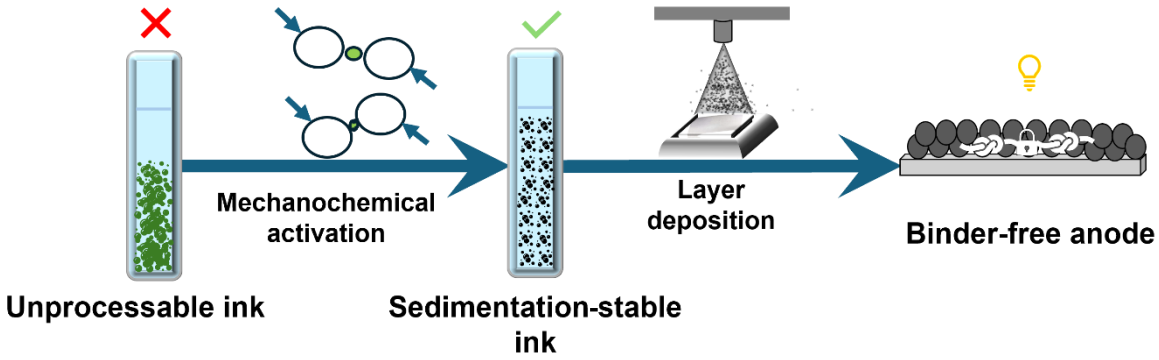

Figure 1 Schematic illustration of the strategy for nanomaterial processing to fabricate sedimentation-stable inks, and binder-free anodes.

This systematic approach integrates structured data on powder and ink properties, the resulting anode layer microstructure data on wetting and mechanical stability, and OER performance data. It enabled us to understand why and how binder-free anodes with an activity superior to that of the feed material can be prepared from comparatively cheap metal oxides by stirred media milling in the liquid phase.

3.1.1 Powder analysis: Size reduction and surface activation

This section presents the detailed characterization of the ball milled NiO, beginning with TEM analysis to assess particle size and morphology, together with BET analysis to determine the specific surface area. Following this, XRD is employed to determine crystalline structure, phase composition, and crystallite size. Finally, Raman spectroscopy is utilized to analyze the vibrational modes, for getting insights into the material's structural order and phase composition.

The first notable observation when comparing materials before and after ball milling was the distinct color change of NiO from dark green to dark grey across the two experimental settings analyzed (Figure S1). This already points towards a change in the stoichiometric ratio of Ni and oxygen within the lattice[44–46]. Figure 2a-c shows the TEM micrographs at lower magnification, with insets providing more magnified views of the NiO feed and ball-milled samples, P-0.3 and P-2.5, respectively. Furthermore, particle size distributions derived from multiple TEM micrographs are shown in Figure 2d-f, which provide a quantitative assessment of particle morphology and size variation. The TEM images of the untreated NiO sample reveal a bimodal particle size distribution, characterized by smaller primary particles (~50 nm) and larger agglomerates ranging from 120 to 220 nm, as observed in the particle size histogram.

In contrast, for the ball-milled samples, the insets clearly show that agglomeration is significantly less. Specifically, P-0.3 and P-2.5 exhibit clearly reduced agglomeration, and individual particles are more distinctly observed. The primary particle size decreased to 11.2 ± 0.5 nm for P-0.3, and 8.8 ± 0.3 nm for P-2.5, respectively, while the shape of the particle size distribution was Gaussian for both ball-milled samples. This is in line with the N_2 adsorption-desorption isotherms for NiO, P-0.3, and P-2.5, presented in Figure 2g. The isotherms corresponding to the ball-milled samples (P-0.3 and P-2.5) exhibit type IV characteristics, as per the IUPAC classification, which are indicative of mesoporous structures[47]. These isotherms were employed to evaluate the specific surface areas of the respective samples using the BET method. A comparison of the calculated surface areas is provided in Table 1.

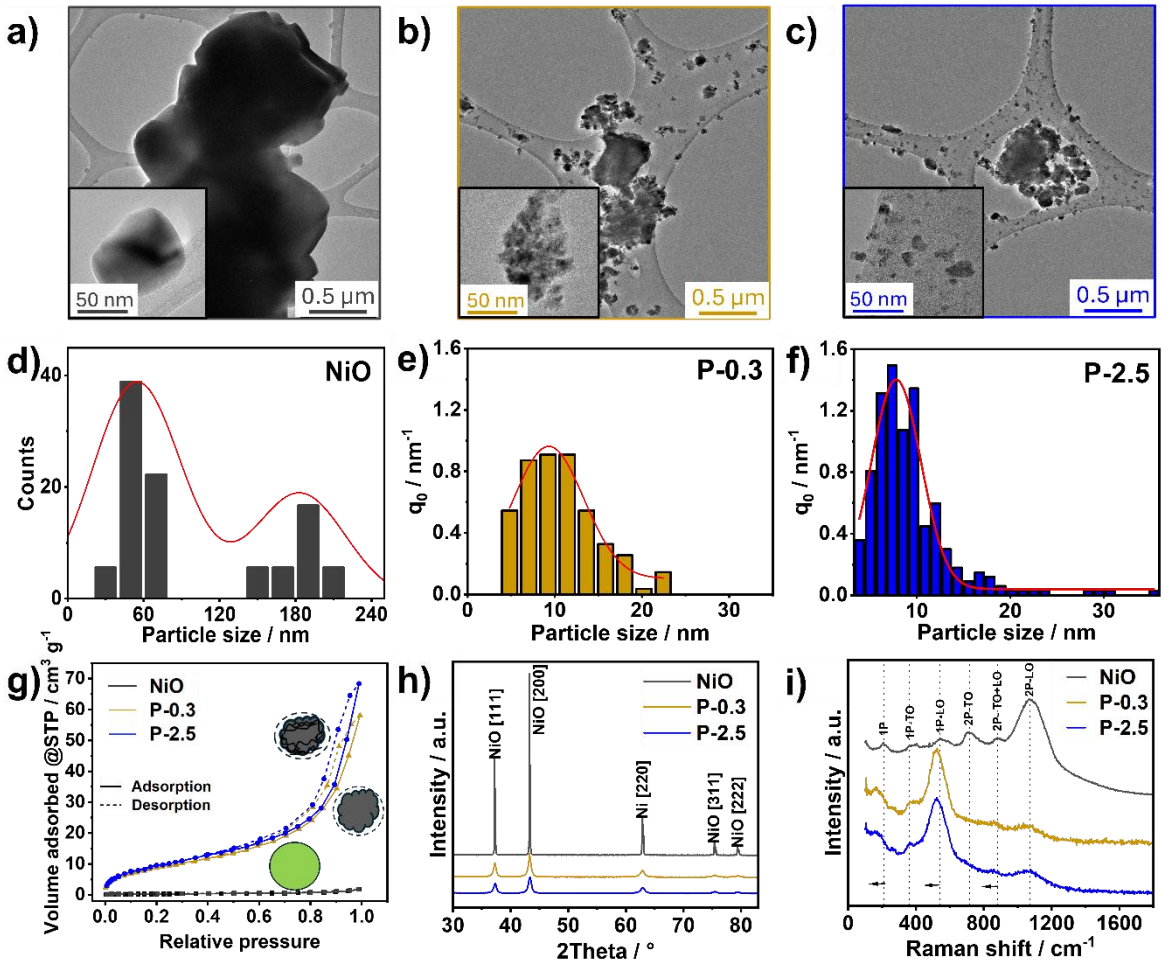

Figure 2 Powder characterization: TEM images at lower and (insets) higher magnifications of (a) NiO, (b) sample P-0.3, and (c) sample P-2.5 with (d), (e), (f) their corresponding particle size distributions. (g) N_2 adsorption and desorption isotherms, (h) XRD spectra, and (i) Raman spectra.

Moreover, Figure 2h depicts the XRD patterns (PDF #01-071-6719) of the pristine NiO and ball milled powders[46]. Here, all samples exhibit characteristic peaks corresponding to the reflection from the [111], [200], [220], [311], and [222] planes, indicating the presence of the face-centered cubic (FCC) structure of NiO[48]. The pristine NiO powder displayed sharper and narrower peaks, reflecting its well-crystallized cubic structure. In contrast, the ball-milled powders exhibited broader peaks. The degree of peak broadening and intensity reduction increased progressively from pristine NiO to P-0.3 and further to P-2.5. While the cubic phase remained predominant in all samples, ball milling introduced a mixture of cubic and distorted phases, with P-2.5 showing more pronounced distortion[49]. To quantify the structural features, we calculated the crystallite size and crystallinity index. The calculated crystallite sizes are

46.9, 12.4, and 11.4 nm, the crystallinity indices are 0.99, 0.94, and 0.92 for NiO, P-0.3, and P-2.5, respectively. Similarly, the lattice microstrain (ε) increased from 2.0 x 10^{-3} for pristine NiO, to 7.5 x 10^{-3} for P-0.3, and 8.2 x 10^{-3} for P-2.5. This underpins that ball milling led to a reduction in crystallite size, a decrease in crystallinity index, and an increase in lattice microstrain.

In line with the analysis of TEM, N_2 sorption, and XRD patterns, also the Raman spectra shown in Figure 2i further underpin structural changes. The spectrum for NiO (black curve) exhibits a prominent Raman band around 1100 cm^{-1}, which is characteristic of the two-phonon longitudinal optical (LO) mode in NiO[50]. This band corresponds to the vibration of Ni ions against oxygen ions within the crystal lattice. For the ball-milled samples P-0.3 and P-2.5, the intensity of the primary peak at 550 cm^{-1} enhanced including the Raman shift to lower wavenumbers and additional broadening, indicating an increased disorder and amorphization due to the ball milling process[51,52]. Table 1 summarizes the type of particle size distribution, primary particle size, crystallite size, crystallinity index, lattice microstrain (refer to Section 2.5.2 for more details), and the BET specific surface area (refer to Section 2.4.5 and Table S1 for more details).

Table 1 Physicochemical characteristics of NiO, P-0.3, and P-2.5 powder samples. The type of particle size distribution, mean primary particle size, specific surface area, crystallite size, crystallinity index, and lattice microstrain were derived from TEM, N_2 sorption, and XRD analysis.

Sam-ple	Type of particle size distribution	Mean primary particle size (nm)	Specific surface area (m^2 g^{-1})	Crystallite size (nm)	Crystallinity index (-)	Lattice micro-strain (-)
NiO	Bimodal	52.2,183.9	3.5	46.9	0.99	2.0 x 10^{-3}
P-0.3	Gaussian	11.2	46.4	12.4	0.94	7.5 x 10^{-3}
P-2.5	Gaussian	8.8	52.2	11.4	0.92	8.2 x 10^{-3}

Based on these results, we conclude the following:

- First, ball milling significantly reduced the particle size, with pristine NiO exhibiting a bimodal particle size distribution (primary particles around 50 nm, agglomerates in the range of 120–220 nm). Upon ball milling, samples P-0.3 and P-2.5 showed uniform primary particle sizes of 11.2 ± 0.5 nm and 8.8 ± 0.3 nm, respectively, as determined by manual analysis of TEM images based on the diameter of clearly distinguishable particles and trend-wise confirmed by the specific surface area. The specific surface area increased substantially from 3.52 m^2 g^{-1} (pristine NiO) to 46.45 m^2 g^{-1} (P-0.3) and 52.25 m^2 g^{-1} (P-2.5). This increase correlates with the reduction in particle size and the elimination of large agglomerates. The increased surface area in P-2.5 reflects the higher impact energy input during milling, enhancing fragmentation and exposure of surface-active sites.

Contrary to conventional milling theory, where smaller beads typically yield finer particles due to higher specific energy input, our results revealed that P-0.3 (processed with 0.3 mm beads) produced slightly larger average particle sizes compared to P-2.5 (2.5 mm beads). To rationalize this deviation, the analysis was extended using the mechanistic framework provided by Kwade et al[30]. According to this model, the overall specific energy input during milling is governed by both the stress number (frequency of bead–bead collisions) and stress intensity (energy per collision).

- In the case of P-0.3, the use of smaller beads inherently results in a higher stress number due to the increased frequency of bead–particle interactions, thereby promoting efficient particle fragmentation in the early milling stages. However, as milling progresses, the particle size reduction in P-0.3 plateaus, approaching what is defined as grinding limit[53], or sometimes dynamic equilibrium[54]. At this stage, further input of mechanical energy no longer yields significant reductions in particle size. This is consistent with the notion that the breakage probability diminishes as the particle size approaches the grinding limit as a critical threshold, where no more breakage events are observed and only defect formation proceeds.
- For P-2.5, the lower stress number is offset by a higher stress intensity per collision, resulting from the greater kinetic energy of the larger beads. While this enables effective fragmentation during early stages of milling, it also implies that continued milling beyond the grinding limit contributes less to further size reduction. Instead, the surplus impact energy promotes the generation of crystallographic defects—such as dislocations, vacancies, and lattice distortions—through localized plastic deformation and atomic rearrangement. These effects become particularly relevant once the grinding limit is reached, where further size reduction is negligible, but defect formation proceeds.
- These structural modifications are substantiated by XRD and Raman analysis. XRD data revealed peak broadening and peak intensity reduction, qualitatively highlighting the introduction of strain and defects in the crystal structure during the mechanical impact that is followed by breakage[55]. Pristine NiO particles consisted of multiple crystallites, whereas milling reduced both particle and crystallite sizes, causing polycrystalline particles to fragment first until both, particle and crystallite sizes converged[56].These structural modifications align with findings reported by QS Song et al., who observed that ball milling reduced the crystallite size and increased structural defects, ultimately affecting both the structural and electrochemical characteristics of nickel hydroxide powders[57]. Raman spectroscopy further indicated structural disruption, amorphization, and reduced antiferromagnetism in the ball milled samples[58,59]. The broadening and increased intensity of the Raman peaks (at 550 cm^{-1}) in P-0.3 and P-2.5 are indicative of a decreased phonon coherence length[60] and increased lattice strain, corroborating the XRD findings. P-2.5 exhibited the most pronounced Raman shift and peak broadening, reflecting the highest degree of structural modification.

Building on these insights on the size changes of the material upon milling and its mechanochemical activation, the following section delves into chemical aspects.

3.1.2 Powder analysis: Chemical composition

The quantitative elemental composition analysis by EDX, presented in Figure S2d, reveals significant changes in the content of nickel (Ni_{bulk}) and oxygen (O_{bulk}). The pristine NiO sample exhibited the highest nickel content, while the ball-milled samples (P-0.3 and P-2.5) showed reduced nickel levels with an increased content of oxygen. EDX mapping revealed an increased oxygen and reduced nickel content in ball-milled samples compared to pristine NiO, indicating enhanced oxidation due to greater exposure of nickel sites to air. P-2.5 exhibited the lowest nickel and highest oxygen content, suggesting a more pronounced oxidation relative to P-0.3. These structural changes could be beneficial for achieving high OER performance, as increased oxidation has been reported to enhance the catalytic activity in transition metal oxides[61–63].

To further understand the EDX data with regard to the O_{bulk}, Figure 3a presents the FTIR spectra of pristine NiO, P-0.3, and P-2.5 samples in the 2650–3950 cm^{-1} range, highlighting changes in the OH content. In line with the findings from EDX, the relative bulk hydroxyl (OH_{bulk}) group concentration shows an increment from pristine NiO to P-0.3, with P-2.5 exhibiting the highest overall concentration of OH_{bulk} groups. Moreover, pristine NiO displays a broad peak at 3700 cm^{-1}, typically associated with free hydroxyl groups on the surface, whereas P-0.3 and P-2.5 exhibit broad peaks at 3469 cm^{-1}, corresponding to the hydrogen-bonded -OH stretching of Ni-OH bonds. This indicates pronounced hydroxide incorporation during ball-milling. P-0.3 shows a less intense peak compared to P-2.5, indicating a higher OH_{bulk} in P-2.5. Altogether, this increase in the oxygen content with the bead size is in line with the previous findings on the enhanced mechanochemical activation of P-2.5.

To further understand how this affects the chemical surface states, XPS was performed. High-resolution O1s spectra of the pristine NiO and ball milled samples P-0.3 and P-2.5 were analyzed as shown in Figure 3b-d. In pristine NiO, sharp and well-defined peaks were detected, corresponding to Ni–O (signal at 529.3 eV), defects such as oxygen vacancies[64] (O_{vac}) at 530.4 eV, and the Ni–O–H signal at 531.2 eV. In comparison, the ball-milled samples show significant broadening of the O1s peaks, particularly at higher binding energies.

The comparative analysis of Ni_{bulk}, O_{bulk}, OH_{bulk}, Ni^{3+}, O_{vac}, and surface hydroxyl (OH_{surf}) content is summarized in Figure 3e. A progressive increase in the concentration of O_{bulk} and Ni^{3+} occurs from pristine NiO to sample P-0.3 and sample P-2.5, with P-2.5 exhibiting a slightly higher content of Ni^{3+} than P-0.3. The presence of these high-valent nickel species remains crucial, as Ni^{3+} is widely recognized to facilitate the formation of active oxyhydroxide intermediates in OER[65]. This increase is rather driven by the formation of O_{vac} which increased from pristine NiO to P-0.3 and P-2-5, as part of the defect generation observed in XRD analysis. Accordingly, the amount of both OH_{bulk} and OH_{surf} groups follows a clear trend: it increases from pristine NiO to P-2.5, with P-0.3 showing again a lower concentration relative to P-2.5.

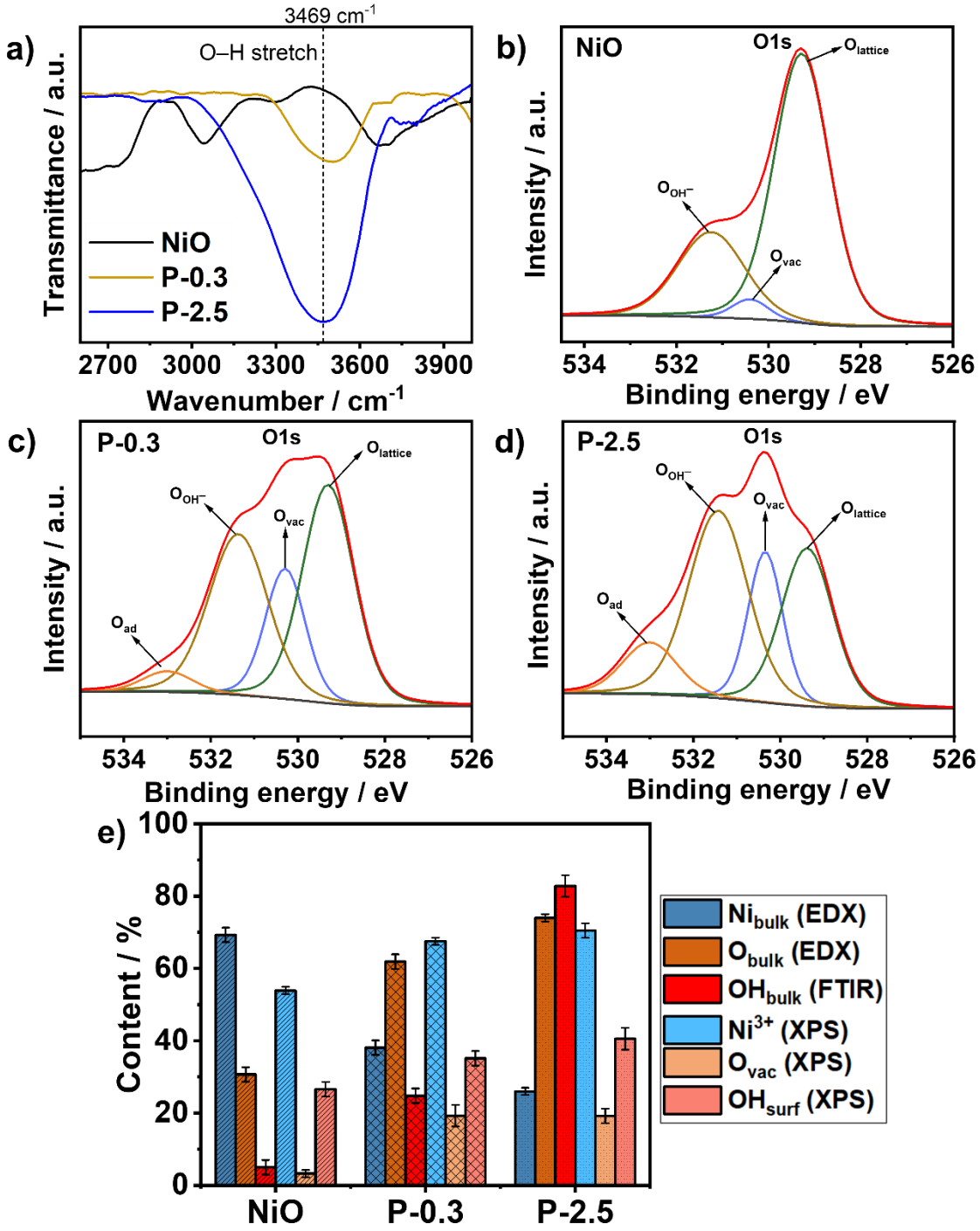

Figure 3 (a) Fourier transform infrared spectra (FTIR) of NiO, P-0.3, and P-2.5 recorded within the 2650–3950 cm⁻¹ range, showcasing differences in OH_{bulk} groups. XPS spectra and their deconvolutions highlighting the O1s region for (b) NiO, (c) P-0.3, and (d) P-2.5, illustrating the variations in surface oxygen species. (e) Comparative analysis of Ni_{bulk} and O_{bulk} from EDX, relative OH_{bulk} derived from FTIR spectra, and Ni^{3+} content, O_{vac}, and OH_{surf} species from O1s spectra for NiO, P-0.3, and P-2.5, indicating their surface and bulk chemical compositions.

In conclusion, ball milling progressively transforms NiO, with P-0.3 representing an intermediate level of mechanochemical activation and structural stability, and P-2.5 showing the most pronounced reduction in crystallite size, surface area enhancement, and oxygen content in both, bulk and surface. These findings set the foundation for analyzing the impact of the particles' mechanochemical activation on dispersibility, anode layer properties, and electrochemical performance.

3.1.3 Dispersion studies

Building on the characterization of NiO and ball-milled powders, it is essential to examine how these structural and compositional changes influence their dispersion behavior. The interaction between the particles and solvents determines their dispersibility, stability against agglomeration, and hence the processability for coating applications. Therefore, pH-dependent zeta potentials and HSP were assessed. As previously noted, pristine NiO exhibited poor dispersion stability, preventing the formulation of a stable dispersion. Consequently, the feed material had to be discarded at this stage.

The zeta potential vs. pH measurements, shown in Figure 4a, were conducted in water without background electrolyte to assess the intrinsic electrical double-layer properties and surface charge behavior of the ball-milled samples. The samples were prepared by dispersing the materials in milli-Q water to avoid any ionic interactions. The results revealed that both P-0.3 and P-2.5 exhibited positive zeta potential values, with P-0.3 having a lower zeta potential in its order of magnitude than P-2.5. Additionally, the bulk pH of the P-2.5-based dispersion of 5.5 was significantly lower than that of P-0.3 with a value of 6.8, indicating a stronger acidic character. This is in line with both the higher zeta potential observed for P-2.5, that points towards an increased surface charge density, and the XPS data, that support a higher concentration of ionizable functional groups in case of P-2.5, such as -OH groups and metal-oxygen species (Ni-OH, Ni^{3+}-O)[66]. The lower pH upon dispersion of the P-2.5 powder in milli-Q water indicates a stronger interaction of the particle surface with protons in the solution, further contributing to its increased surface charge[67]. This implies that the higher impact energy in P-2.5 resulted in more exposed reactive sites, enhancing proton adsorption and leading to greater electrostatic stabilization of the particles against agglomeration[68]. However, despite their positive zeta potentials, the dispersions were not long-term stable in water, as agglomeration-induced sedimentation occurred within an hour at earth gravity. Ions cannot be added via a background electrolyte to the dispersion as they might affect the OER. Therefore, water-based inks were discarded and the suitability of small-chain organic solvents was analyzed.

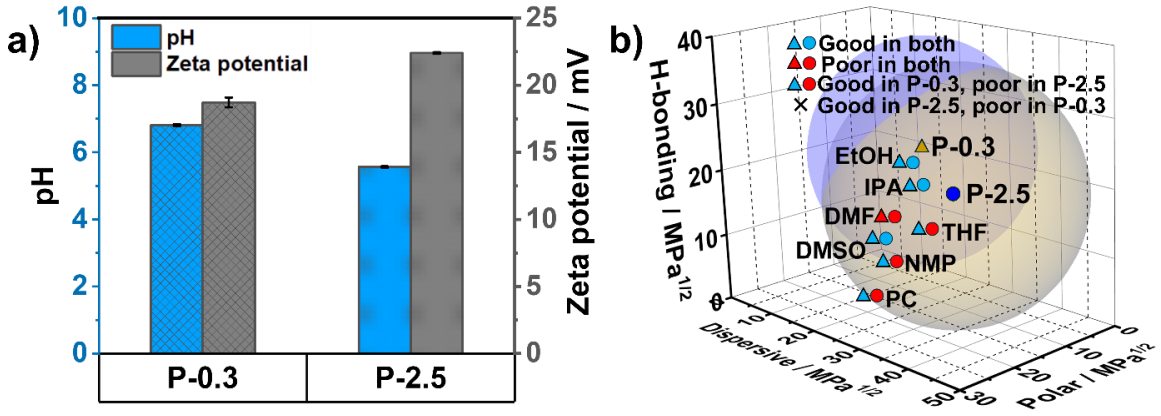

Figure 4 (a) pH-dependent zeta potential values of P-0.3 and P-2.5, indicating differences in the surface charge behavior. (b) HSP spheres illustrating the dispersive (δD), polar (δP), and hydrogen bonding (δH) interactions for P-0.3 and P-2.5, providing insight into their solvent compatibility and polarity. Light blue coloration represents good solvents, whereas red coloration indicates poor solvents.

The surface properties of nanoparticles dictate their interactions with solvent molecules, thereby determining their dispersion behavior and colloidal stability in organic solvents. According to the concept of HSP following the paradigm of like disperses like, the interaction between probe liquids and catalyst particles can be described using three key parameters: dispersive forces (δD), dipolar intermolecular forces (δP), and hydrogen bonding (δH), which together define coordinates in the three-dimensional Hansen space. Therefore, HSP analysis enables the strategic selection of an appropriate continuous phase for catalyst ink formulations.

In alignment with previous studies, the two-step strategy proposed by Amin et al. was employed to select suitable probe liquids[31]. Dispersions with P-0.3 remained stable in EtOH and THF from the first step, while in the second step, additional solvents such as IPA, DMSO, NMP, and PC were found as good probe liquids, with DMF being the only poor probe liquid. In contrast, P-2.5 showed a more selective behavior, with only EtOH forming a stable dispersion in the first step, and in the second step, only IPA and DMSO were found to be good probe liquids.

Following this, HSP were determined by ranking the probe liquids according to their relative sedimentation times (Table S3), following the method developed by Süß et al.[39]. As shown in Figure 4b, P-0.3 exhibited a higher δD than P-2.5, while P-2.5 demonstrated higher δP and δH parameters compared to P-0.3. The elevated δP and δH values in P-2.5 indicate stronger interactions with polar solvents and hydrogen-bonding species, resulting in its selective compatibility with DMSO and IPA. Conversely, the higher δD value in P-0.3 reflects enhanced interactions with probe liquids dominated by dispersive forces, such as NMP and PC, enabling compatibility with a broader spectrum of solvents.

The zeta potential measurements and HSP analysis demonstrated the particle surface-solvent-interactions for the ball milled samples. Based on the results, we summarize as follows:

- P-0.3 displayed lower zeta potential values, suggesting a more balanced surface charge distribution. In contrast, P-2.5 exhibited a higher zeta potential at lower pH, indicating a greater concentration of protonated ionizable surface groups, leading to stronger electrostatic stabilization in aqueous dispersions.
- The HSP analysis further supports these distinctions. P-0.3, with a larger HSP sphere radius, exhibited broader compatibility with various probe liquids. Whereas, P-2.5 had a smaller HSP sphere radius with higher δP and δH parameters, indicating stronger hydrogen-bonding interactions and selective dispersibility in only a few probe liquids. Furthermore, the elevated polar component in P-2.5 indicates a more electronegative surface, which could enhance its affinity for the adsorption of foreign species[69].

Among all the probe liquids evaluated, IPA demonstrated superior dispersion characteristics among the polar protic solvents. Consequently, and also due to its low cost and toxicity compared to polar aprotic solvents used, pure IPA was selected as the continuous phase for subsequent ink preparation and coating.

3.2 Ink formulation and stability

Figure 5 shows the transmittograms for inks based on P-0.3 and P-2.5 which provide a direct visualization of sedimentation time, radial position, and transmission changes over time.

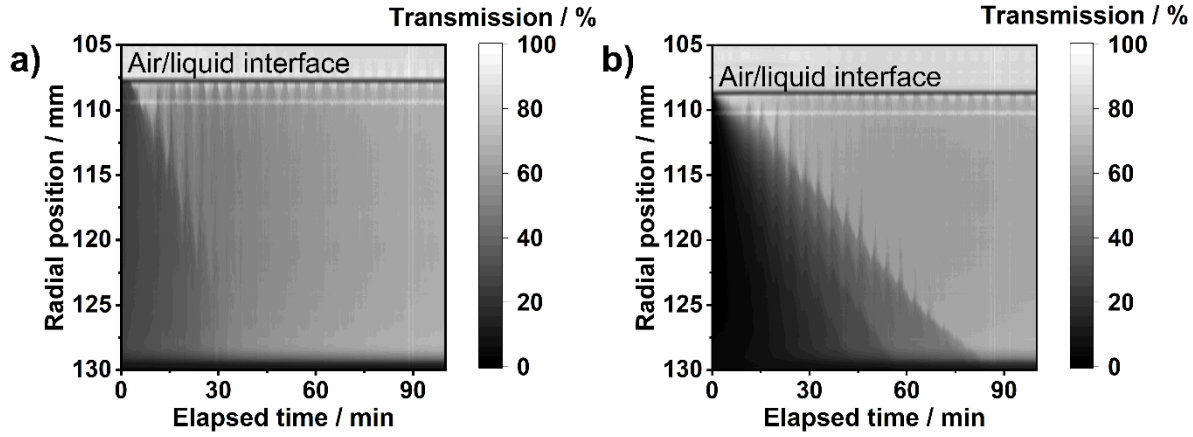

Figure 5 Transmission profiles converted into transmittograms for inks based on (a) P-0.3 and (b) P-2.5, both dispersed in IPA (1 mg mL^{-1}). The transmittograms illustrate the sedimentation behavior over time (x-axis) and radial position (y-axis), with the transmission intensity represented by the variation in color intensity.

Measurements were conducted at 1500 rpm, corresponding to 330 times the gravitational acceleration, hence, both, P-0.3- and P-2.5-based inks can be regarded as sufficiently sedimentation-stable to generate a reliable coating at gravity. However, transmittogram-analysis revealed distinct sedimentation behaviors between the samples. Inks based on P-0.3 exhibited bulk sedimentation, with the entire particle population settling uniformly within the first 30 min, after which no further significant settling occurred. In contrast, inks based on P-2.5 demonstrated a markedly higher sedimentation stability, with the settling process extending to ~80 min. To contextualize these findings, under normal gravitational conditions, P-0.3 would require approximately 11 days to completely sediment, whereas P-2.5 would need around 18 days if no agglomeration occurs. For a comprehensive quantitative assessment, we refer to the S-scores shown in Figure S6b (supplementary information). Similar to Dwari et al.[70], who found that hydroxyl groups and H-bonding facilitated the guar gum adsorption and improved the sedimentation time for kaolinite dispersions, the enhanced stability of P-2.5 against agglomeration can be attributed to its higher OH_{bulk} content and high δH value. Compared to P-0.3, the P-2.5 powder exhibits stronger particle-solvent interactions in IPA that effectively mitigate agglomeration. The next section examines how these improved ink formulations influence coating characteristics and what this implies for electrode fabrication.

3.3 Coating characterization

3.3.1 Microstructure of the layers

Figure 6 presents the morphological characterization of anodes fabricated using inks based on P-0.3 and P-2.5 (refer to the Experimental Section for more details), examined through the analysis of 3D profilometry images. Anodes based on sample P-0.3 (shown in Figure 6a) show slightly larger particle assemblies on the substrate that formed during drying compared to anodes based on P-2.5 (shown in Figure 6b). This is in agreement with SEM images (shown in Figure S7a-b) where P-0.3 exhibits a highly inhomogeneous surface with pronounced particle agglomeration, whereas P-2.5 exhibits a more uniform morphology with reduced agglomerate size and improved surface coverage. In terms of quantitative numbers, the root mean square surface roughness was calculated which however results in almost the same mean value for anodes based on P-0.3 and P-2.5, with a slightly larger standard deviation in case of P-2.5.

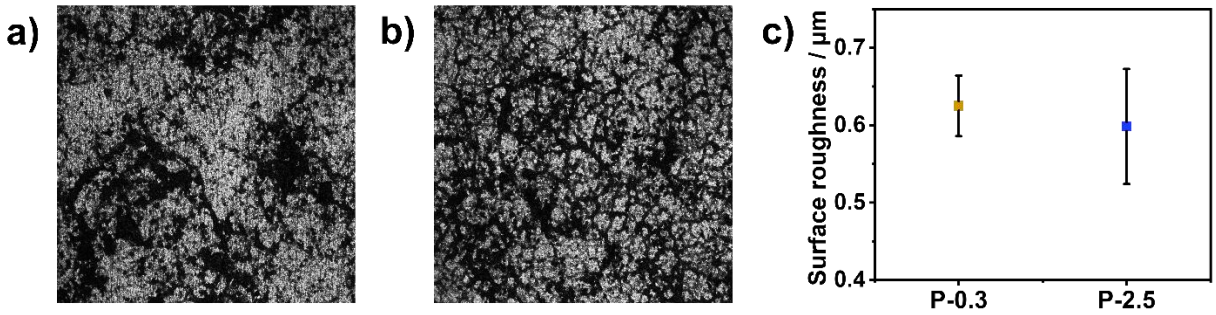

Figure 6 Three-dimensional profilometer images with 300x300 µm² area illustrating the surface topography of spray-coated anodes fabricated by ultrasonic spray-coating of inks based on (a) P-0.3 and (b) P-2.5 particles on a Ni plate substrate. (c) Quantitative surface roughness analysis (root mean square values) of the coated samples, with five measurement points for both P-0.3-based and P-2.5-based coatings.

Having assessed the physical structure of the layers, it is essential to examine their chemical composition to determine whether the coating process induced any changes in the material itself[71]. To compare anode layer properties with powder features, we used XRD, EDX, and XPS to assess potential modifications in oxidation states, and chemical interactions resulting from the deposition process.

3.3.2 Chemical properties of anode layers

Figure 7a presents the XRD patterns of the spray-coated samples, designated as P-0.3 and P-2.5. Both patterns exhibit diffraction peaks corresponding to NiO, which are consistent with those observed in their respective powder samples, confirming the phase retention post-deposition. The primary distinction in the coated samples arises from the additional diffraction signals originating from the underlying Ni substrate. Specifically, prominent reflections corresponding to the (111), (200), and (220) crystallographic planes of metallic Ni are observed, as indexed by the JCPDS card no. 04-0850.

Figure 7b illustrates the quantification of Ni_{bulk} and O_{bulk} contents obtained from EDX measurements, along with Ni^{3+}, O_{vac}, and OH_{surf} species derived from the deconvolution of the Ni 2p and O 1s XPS spectra (shown in Figure S8). EDX analysis reveals comparable Ni_{bulk} content for both P-0.3 and P-2.5 samples (approximately 35 at.%), but a significant increase in O_{bulk} is observed, from ~34 at.% in P-0.3 to ~45 at.% in P-2.5, representing a relative rise of more than 10 at.%. Unfortunately, based on the powder analysis – the most-interesting OH_{bulk} could not be directly measured in the anode layers, due to the thin and morphologically irregular catalyst coatings that limit the probing depth and signal intensity in FTIR analysis. The XPS-derived analysis shows that Ni^{3+}, O_{vac}, and OH_{surf} contents remain largely similar between the two samples, with OH_{surf} even exhibiting a slight decrease in P-2.5. Given that surface oxygen species remain largely unchanged while the signal of O_{bulk} increases substantially, it is reasonable to hypothesize that this increase in O_{bulk} is primarily attributable to an enhanced OH_{bulk} concentration in P-2.5.

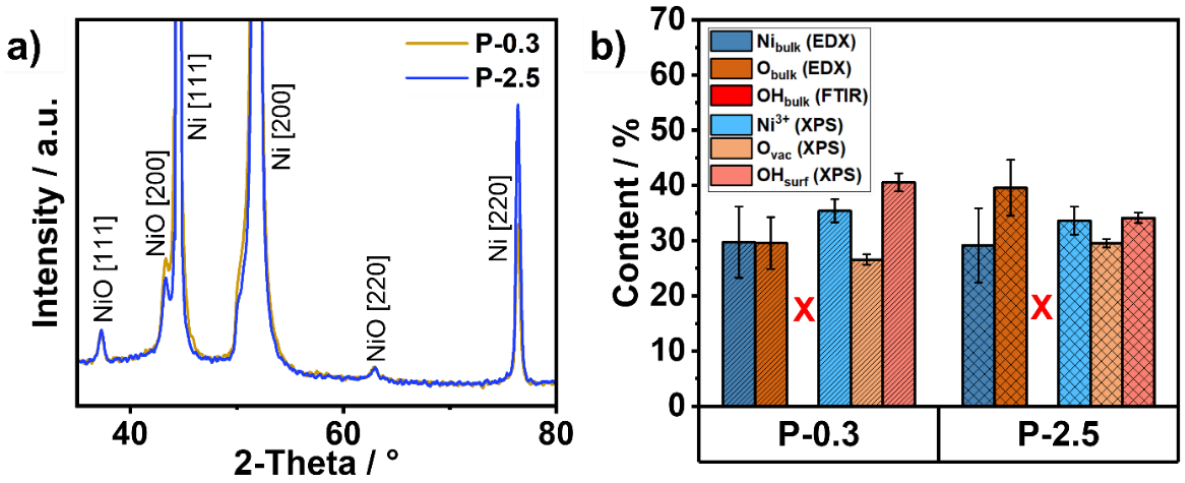

Figure 7 (a) XRD patterns for spray coated anodes based on P-0.3 and P-2.5. (b) Comparative analysis of Ni_{bulk} and O_{bulk} from EDX, an "X" indicating the missing, not detectable information on the relative OH_{bulk} derived from the FTIR spectra, and the content of Ni^{3+}, O_{vac}, and OH_{surf} species derived from the O1s spectra of spray coated P-0.3 and P-2.5 anode layers.

3.3.3 Anode layer properties: Wetting and mechanical stability

After assessing the microstructure, we now examine anode layer properties. The contact angle measurements shown in Figure 8a provide insight into the initial wettability of the coated samples. The results show that P-0.3-based anodes have a contact angle of 126.2 ° ± 0.15 ° and P-2.5-based anodes have a contact angle of 111.5 °± 0.55 ° when measured with 1 M KOH. This implies that both anodes are lyophobic[72]. Noteworthy, and in line with our findings on the increased OH_{bulk} content in the particle bulk (see Figure 3e), the intrinsically lyophilic pristine NiO[73] transformed into a lyophobic material after ball milling.

Our previous study explored lyophobic anodes, defined by the Cassie-Baxter model for porous anode layers, demonstrating their influence on bubble detachment dynamics[71,74]. However, due to the distinct intrinsic chemical properties of P-0.3 and P-2.5 (refer to Section 3.1.2), the wetting behavior cannot be fully described by the Cassie–Baxter model alone. Although both coatings exhibit similar surface roughness, P-2.5 displays a lower contact angle, suggesting enhanced intrinsic wettability. This is attributed to its rather likely higher OH_{bulk} content which increases the surface polarity and the density of active sites for electrolyte interaction and O_2 gas release[75]. These characteristics promote an improved solid–liquid contact and reduce air entrapment beneath the droplet. The data point towards the occurrence of a Cassie–Wenzel transitional regime, but the observed difference in wettability is governed primarily by chemical surface properties and only slightly affected by the small differences in the microstructure discussed in the previous chapter.

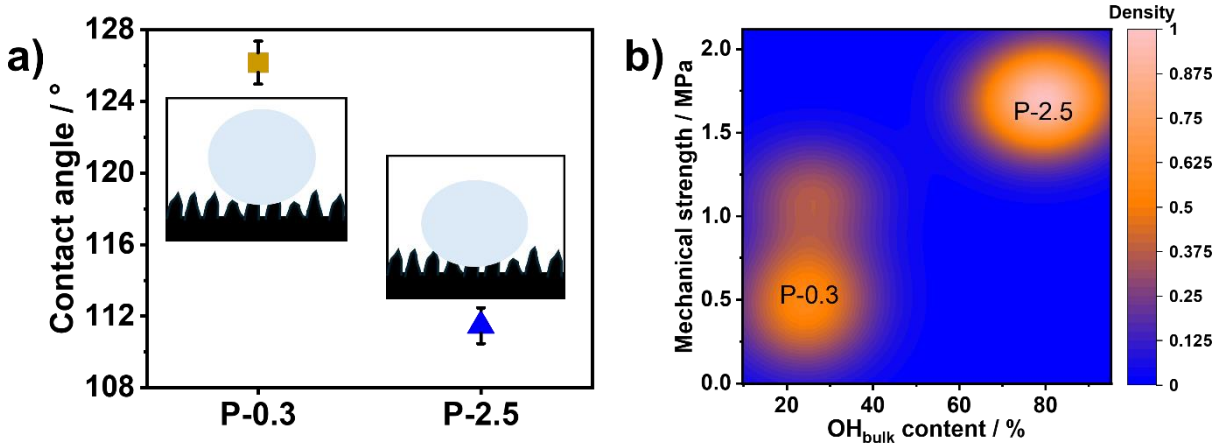

Figure 8 (a) Contact angle measurements with 1 M KOH for spray coated anodes based on samples P-0.3 and P-2.5. (b) 2D plot of the mechanical strength (from adhesion analysis on spray coated electrodes) and OH_{bulk} content (from powder FTIR as FTIR on layers is not possible) for samples P-0.3 and P-2.5.

Data on the mechanical stability as the second OER-relevant layer property is shown in Figure 8b. The results reveal a significant difference in the adhesion strength between the two samples, with anodes based on P-0.3 exhibiting a significantly lower adhesion strength (0.37 ± 0.44 MPa) than anodes based on P-2.5 displaying a nearly fivefold higher adhesion strength (1.69 ± 0.06 MPa). In both cases, the failure mechanism was identified as adhesive failure, indicating that the mechanical cohesion between individual particles is stronger than the adhesion between the particle layer and the Ni support.

The reason for this difference can be explained as follows: Firstly, the P-2.5 powder exhibits a higher specific surface area, which likely results in an increased number of contact points between the powder particles and the nickel substrate. This enhanced interfacial contact can be advantageous for improving the mechanical anchoring of the catalyst layer. Secondly, the OH groups play a dual role. They improve wetting and droplet spreading during the coating process, and they may enhance interparticle cohesion and adhesion between the anode layer and the substrate, potentially through hydrogen bonding interactions. These effects collectively contribute to the improved mechanical stability of the coated layer. Xiao et al. reported a similar trend in the context of solid-state battery cathodes, where an increased OH content was found to reduce the Young's modulus. This reduction in mechanical stiffness improved the conformal contact between the solid electrolyte and the electrode materials, leading to the formation of a robust and stable interfacial layer and, consequently, enhanced the cycling stability[76]. In the context of this work, Figure 8b illustrates a positive correlation between the OH_{bulk} content assessed by FTIR measurements on powder samples (as the signal was undetectable for the coated layers) and the adhesion strength. This correlation highlights the critical role of OH_{bulk} content in controlling the interfacial mechanical behavior between the catalyst layer and the nickel substrate. In contrast, the OH_{surf} content exhibited slight variations across the P-0.3, and P-2.5 samples (refer to Section 3.3.2), and thus did not significantly contribute to the observed differences in adhesion.

The data suggest that in particular a higher concentration of OH_{bulk} groups enhances the chemical affinity between the nanoparticles and the substrate interface, likely through hydrogen bonding and polar interactions (also refer to the HSP discussed in Section 3.1.3), which could contribute to stronger interfacial bonding and improved cohesion within the catalyst layer as well as adhesion to the substrate. Notably, the measured adhesion strengths

for both P-0.3 and P-2.5 exceed the threshold stress values identified in simulation studies by Igwe et al., which determined a maximum stress value of 0.143 MPa for water electrolysis[77]. This indicates that the binder-free NiO coatings provide promising mechanical stability worth being further investigated.

So far, we have uncovered a pathway for developing binder-free electrodes through mechanochemical activation. We understood how induced defects and increased surface area significantly improved the mechanical stability of anode layers, eliminating the need for polymeric binders. Before moving on with the electrochemical analysis, we want to build upon these findings and exploit this understanding by transferring it to an industrially more relevant scenario than planetary ball milling—catalyst powder comminution with a stirred media mill.

3.4 Method exploitation by stirred media milling

To validate the binder-free anode fabrication via mechanochemical activation, commercial NiO was subjected to stirred media milling in IPA, resulting in a sample that will be denoted as S-0.3 in the following (details in the Experimental Section 2.2). Stirred media milling as a method was chosen because it enables direct operation in the liquid phase and supports continuous processing. This makes it well-suited for scalable, industrial applications[78]. Dispersibility studies on the ball milled powders unraveled IPA as the most-compatible solvent where NiO is intrinsically stable. Therefore, pure IPA was selected as continuous phase for the liquid phase comminution process to minimize reagglomeration.

TEM images of the dried powder after stirred media milling (Figure 9a) revealed significant morphological transformations. While the untreated NiO exhibited a compact crystalline structure, and P-0.3 and P-2.5 showed more distinct individual particles, sample S-0.3 displays a highly fragmented morphology. This structural change enhances the surface area and points towards pronounced defect formation. This is further confirmed by the XRD data depicted in Figure 9b which indicates pronounced peak broadening in S-0.3 relative to P-0.3 and P-2.5.

Figure 9c presents the quantitative analysis of both bulk and surface chemical compositions for the P-0.3, P-2.5, and S-0.3 powder samples. The data integrates Ni_{bulk} and O_{bulk} contents obtained from EDX, OH_{bulk} content from FTIR, and the surface chemical species from deconvolution of the XPS spectra, Ni^{3+}, O_{vac}, and OH_{surf}. EDX analysis revealed that the Ni_{bulk} content of sample S-0.3 was comparable to P-0.3 and relatively higher in comparison to the P-2.5 sample. Conversely, the O_{bulk} content was lower in S-0.3 and P-0.3 than in case of P-2.5. In contrast, quantitative analysis of the FTIR spectra revealed a markedly elevated and outstanding relative OH_{bulk} concentration in the S-0.3 sample, with an approximately 7–8-fold increase relative to P-2.5 and P-0.3 powders (Figure S9). Quantitative deconvolution of the O1s XPS spectra (Figure S10) confirmed that the concentrations of Ni^{3+}, O_{vac}, and OH_{surf} species were comparable across all three investigated materials.

Following this, the S-0.3 ink (diluted to 1 mg mL^{-1}) was uniformly deposited onto a Ni substrate via spray coating under identical processing conditions and with the same mass loading as in case of inks obtained from P-0.3- and P-2.5 powders. Accordingly, the SEM images of the S-0.3-based anode (refer to Figure S11) display a markedly smoother and more homogeneous surface with finely distributed features, reflecting the structuring effect achieved through stirred media milling. Surface topography analysis using 3D optical profilometry (Figure 9d) further indicates macroscopically homogeneous layers and the root mean square roughness values are comparable across all samples independent of their comminution process (see Figure S12).

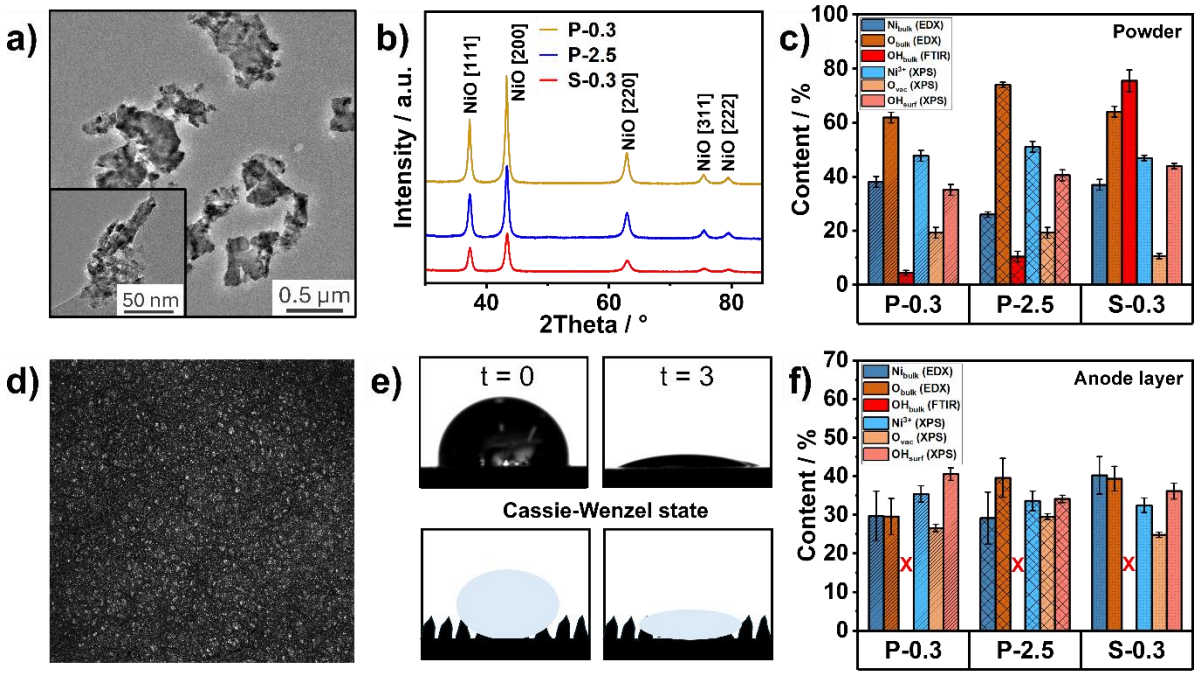

Figure 9 a) TEM images of sample S-0.3, illustrating both low- and high-magnification views, highlighting the morphology and microstructural features. b) XRD patterns of P-0.3, P-2.5, and S-0.3 powders, showing the presence of distinct NiO phases. c) Comparative bulk and surface chemical composition analysis of P-0.3, P-2.5, and S-0.3 powders: Ni_{bulk} and O_{bulk} content from EDX, OH_{bulk} content, and Ni^{3+} content, O_{vac}, and OH_{surf} species from O1s spectra. d) Three-dimensional optical profilometry image with 300x300 µm² area of the spray-coated anode layer based on sample S-0.3, exhibiting its surface topography and uniformity. e) Contact angle measurements of the S-0.3 coating at t = 0 min and t = 3 min, accompanied by schematic representations illustrating the evolution of wettability over time. f) Bulk and surface chemical composition analysis of spray-coated P-0.3, P-2.5, and S-0.3 samples.

Contact angle measurements (Figure 9e) demonstrate that S-0.3-anodes exhibit enhanced lyophilicity compared to anodes made of P-0.3 and P-2.5, respectively. At t = 0, the KOH droplet initially remains in the Cassie-Baxter state with a contact angle of 103° but transitions into the Wenzel regime (contact angle < 90°) over time, completely spreading within 3 min. This aligns with the speculated observation for P-2.5, which had a lower contact angle compared to P-0.3. This behavior highlights the clearly improved wetting characteristics of S-0.3 relative to P-2.5 and P-0.3, likely attributable to its significantly higher OH_{bulk} content present in the S-0.3 powder. These enhance the lyophilic nature of the surface and promote stronger interactions between the anode layer and the aqueous KOH used as electrolyte.

Finally, the chemical composition of the anode layers based on P-0.3, P-2.5, and S-0.3 is shown in Figure 9f. EDX elemental analysis indicated a relatively higher Ni_{bulk} content in S-0.3 compared to P-0.3 and P-2.5 counterparts, whereas the O_{bulk} content in S-0.3 was comparable to P-2.5 and relatively lower when compared to P-0.3-based anodes. The surface composition, determined with XPS analysis showed that the concentration of Ni^{3+}, O_{vac}, and OH_{surf} remained consistent across all three anodes.

In summary, the mechanochemical activation of NiO via stirred media milling in liquid IPA profoundly transformed the microstructural and chemical characteristics of the material. Powder S-0.3 that originated from stirred media milling demonstrated the highest OH_{bulk} content (unfortunately not confirmable in the corresponding anode because of the low layer thickness, hindered reliable FTIR measurement) and a substantially enhanced lyophilicity in the resulting anode layer, while preserving a relatively uniform surface structure. The increased

peak broadening observed in the XRD spectra reflects a higher lattice microstrain in S-0.3 (8.8 x 10^{-3}) compared to P-0.3 (7.5 x 10^{-3}) and P-2.5 (8.2 x 10^{-3}), indicative of extensive structural fragmentation. Despite having comparable surface compositions in the deposited layers, the combination of bulk chemical modification and microstructural changes is expected to significantly improve charge transfer and mass transport properties, contributing to an enhanced electrocatalytic performance for OER. Therefore, in the following section, we investigate the electrochemical performance of powders and binder-free anodes, focusing on both the intrinsic activity of the materials and their resulting catalyst layers.

3.5 Electrochemical performance

RDE measurements were conducted to evaluate the electrocatalytic activity and short-term stability of P-0.3, P-2.5, S-0.3, and pristine NiO under hydrodynamic control. As shown in Figure 10a, the LSV curves indicate that pristine NiO was the least active. Catalyst delamination occurred even at these comparatively mild conditions, which again reflects the generally poor processability of this particular NiO powder. P-0.3 exhibited a slower current increase and required a higher overpotential to reach a given current density (10 mA cm^{-2}), demonstrating a still low catalytic activity. In contrast, P-2.5 showed a steeper current response at lower overpotentials. S-0.3 demonstrated the best electrochemical performance among all samples with the lowest overpotential, reflecting enhanced kinetics. The potential at 10 mA cm^{-2} (E_{10}) was highest for P-0.3 at 1.77 V vs. RHE, followed by P-2.5 at 1.66 V vs. RHE, and lowest for S-0.3 at 1.63 V vs. RHE, confirming its significantly improved activity for the OER.

However, although the electrocatalytic activity of P-0.3 is observed to be lower than that of P-2.5, and S-0.3 looking particularly promising, the ultimate performance of these materials in practical electrolysis conditions is not solely governed by their inherent properties[79]. Therefore, in the following, we also examine the spray-coated anodes to assess structural features that may influence their behavior under more realistic electrolysis conditions.

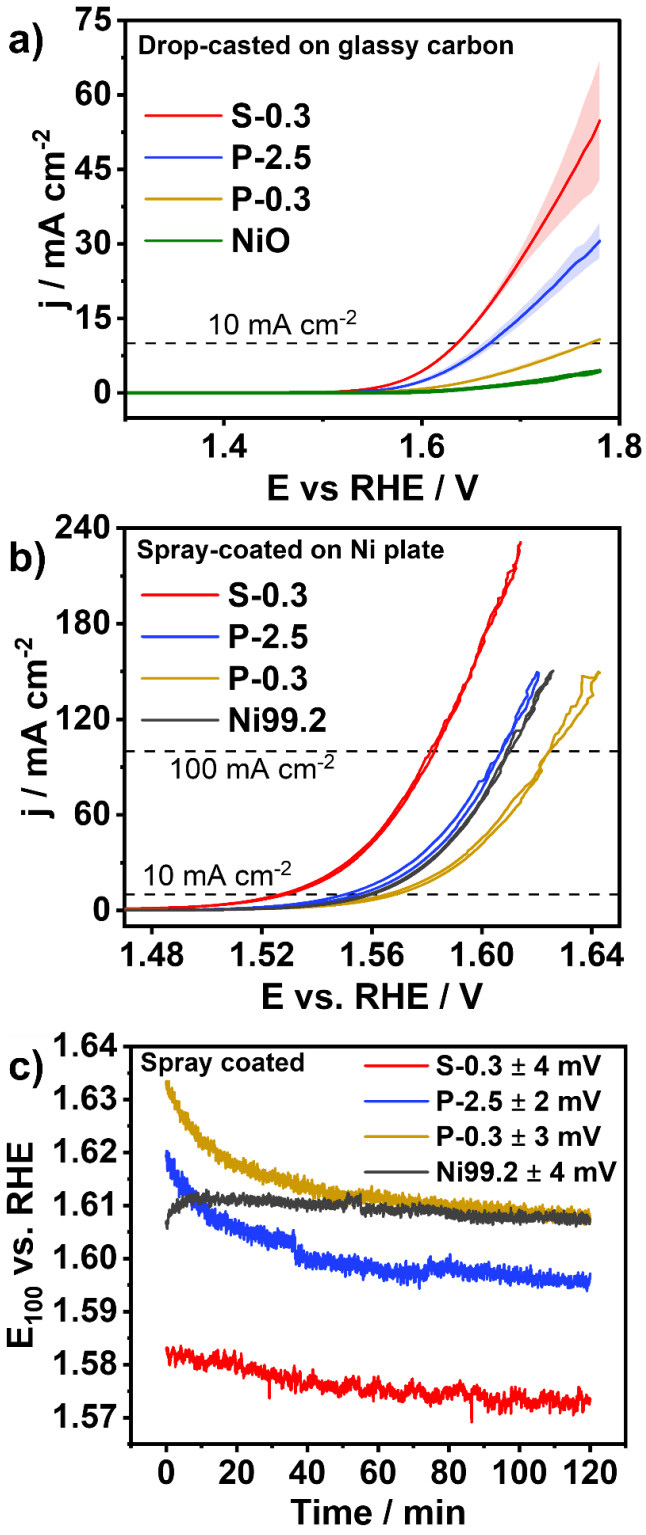

Figure 10 a) Linear sweep voltammograms recorded in 1 M KOH for powder samples P-0.3, P-2.5, S-0.3, and NiO on a rotating disk electrode b) Cyclic voltammograms recorded in 1 M KOH for spray coated samples P-0.3, P-2.5, S-0.3, and the bare Ni99.2 substrate. c) Chronopotentiometry measurements at 100 mA cm^{-2} in 1 M KOH for spray coated samples P-0.3, P-2.5, S-0.3, and the bare Ni99.2 substrate.

The electrochemical performance of the spray-coated P-0.3, P-2.5, and S-0.3 anodes was evaluated using a three-electrode beaker-cell setup in 1 M KOH, with Ni99.2 serving as a reference material. The CV conditioning profiles (shown in Figure S13a) of P-0.3, P-2.5, and S-0.3 were recorded over 50 consecutive cycles to examine the evolution of their redox-active Ni species. All samples displayed prominent redox couples associated with $Ni^{2+} \rightarrow Ni^{3+}$ and $Ni^{3+} \rightarrow Ni^{4+}$ transitions in the potential range of 1.3–1.45 V vs. RHE[71], indicating the formation of higher-valent nickel oxyhydroxide species, which serve as active intermediates for the OER[70]. Despite these shared characteristics, the samples differed significantly in their redox behavior. P-0.3 and P-2.5 displayed nearly identical CV profiles, both exhibiting relatively low current responses. In contrast, S-0.3 demonstrated slightly higher current densities and a small peak shift.

To gain further insights into the electronic and interfacial properties of the anodes, EIS was performed, and the R_u values were determined (Figure S13b). Among all samples, Ni99.2 exhibited the lowest R_u value of 0.15 Ω. In comparison, the spray-coated anodes displayed similar R_u values with resistances of 0.85 Ω, 0.82 Ω, and 0.76 Ω for anodes based on P-0.3, P-2.5, and S-0.3, respectively. The elevated R_u values in P-0.3, P-2.5, and S-0.3 can be ascribed to the intrinsically lower electrical conductivity of nickel oxide relative to metallic nickel.

As shown in Figure 10b, CV curves were recorded, and the overpotentials corresponding to current densities of 10 and 100 mA cm^{-2} were analyzed. At 10 mA cm^{-2}, Ni99.2 and P-0.3 both required an overpotential of 1.56 V vs. RHE, while P-2.5 showed a slightly improved performance at 1.55 V vs. RHE. Notably, S-0.3 exhibited the lowest overpotential of 1.53 V vs. RHE. A similar trend was observed at 100 mA cm^{-2}, in such a way that Ni99.2 and P-0.3 exhibited overpotentials of approximately 1.60 V and 1.62 V vs. RHE, P-2.5 required 1.60 V vs. RHE, and S-0.3 maintained superior performance with an overpotential of 1.58 V vs. RHE.

These findings are supported by the stability (CP) tests at 100 mA cm^{-2}, as shown in Figure 10c. The Ni99.2 substrate exhibited an initial overpotential of 1.61 V vs. RHE, which remained stable throughout the duration of the test. Anodes made of P-0.3 began with the highest overpotential of 1.63 V vs. RHE, gradually activated to a stabilized value near 1.61 V vs. RHE. P-2.5 showed an initial overpotential of ~1.61 V vs. RHE and maintained a slightly lower, stable value of about 1.60 V vs. RHE. Notably, the S-0.3 anode stood out and exhibited the most favorable performance, with an initial overpotential of 1.58 V vs. RHE and stabilizing around 1.57 V vs. RHE, indicating superior catalytic activity.

The observed differences in the electrochemical behavior of P-0.3, P-2.5, and S-0.3 can be attributed to the following reasons:

- The difference in R_u between milled samples and the Ni99.2 substrate is ascribed to the increased density of grain boundaries and the formation of surface oxides induced by the stirred media and ball milling processes.
- At higher current densities, differences in CV and CP curves arise from the variation in the OH content, indicating a higher density of active sites, as supported by specific surface area measurements. P-0.3 initially shows a lower current response due to fewer active sites and slower activation but improves over time, pointing towards progressive activation[80]. S-0.3, with its clearly enhanced hydroxylation, demonstrates superior redox activity and improved ion transport[81]. Additionally, the improved wettability of S-0.3 (refer to Section 3.4) further enhances electrolyte contact, which might help in bubble removal and, thus, contributing to its improved catalytic performance.

Noteworthily and very important, within 2 h of testing, no delamination was monitored for S-0.3, P-2.5, and P-0.3 electrodes, evidencing their chemical and mechanical stability as a binder-free anode layer (SEM images and XPS analysis in supplementary Figure S14-S16). Quantitative analysis of the $Ni2p_{3/2}$ deconvoluted spectra revealed a higher proportion of Ni^{3+} species in P-0.3 and P-2.5 compared to S-0.3. This indicates that S-0.3, with its lower initial Ni^{3+} content, may possess a greater capacity for electrochemical activation through Ni^{2+}/Ni^{3+} redox transitions during operation.

The high mechanical stability against delamination is explained as follows:

- Firstly, the absence of delamination in P-0.3, P-2.5, and S-0.3 coatings arises from an increased number of contact points between the nanostructured oxide particles and the metallic substrate. This is a consequence of the enlarged effective surface area and surface roughness introduced during the ball milling and deposition processes. These surface features promote stronger physical anchoring at the nanoparticle–substrate interface, which enhanced the adhesion strength (refer to Section 3.3.2 for more details).
- Secondly, the hydroxylation of NiO enhances chemical bonding during OER through the formation of a $Ni(OH)_2$ interface, which strengthens the adhesion between the deposited layer and the Ni substrate, further preventing delamination.

The electrochemical analysis confirmed the stability and strong adhesion of P-0.3, P-2.5, and S-0.3 coatings during OER, proving the effectiveness of the mechanochemical activation in producing robust binder-free anodes.

These findings, starting from a commercially available NiO powder, innovate and proof the potential of stirred media milling as a method to significantly enhance the activity of metal oxides. Together with the remarkable mechanical stability of therefrom generated anodes against delamination, a pathway towards binder-free anodes for alkaline water electrolysis is opened.

4. Conclusion

In this work, we demonstrate that mechanochemical activation enables the conversion of unprocessable commercial NiO powders into binder-free anodes for AWE with significantly improved performance. In the first phase of the study, planetary ball milling enabled the preparation of inks that were sufficiently stable against sedimentation to be processed into reproducible anode layers. These anodes yielded a moderate overpotential of 365 mV at 100 mA cm^{-2} in 1 M KOH, however, without any delamination even in the absence of polymeric binders, proving a clearly enhanced mechanical stability. We found that upon ball milling, the physicochemical properties of NiO nanoparticles were fundamentally altered through the creation of lattice defects with enhanced OH_{bulk} content and O_{vac}, surface hydroxylation that mediates particle-particle and particle-substrate interactions, and morphological restructuring, including particle size reduction and surface roughening, that increases the specific surface area and accessible active sites.

In the second part of our study, we demonstrate the successful transfer of the gained understanding to stirred media milling—an industrially relevant wet comminution process that enables the preparation of sedimentation-stable inks in a single step. The resulting electrodes exhibited a reduced overpotential of 343 mV at 100 mA cm^{-2}, along with high mechanical stability These two significant improvements were attributed to the synergistic effects of elevated surface hydroxylation, improved wettability, and strengthened interparticle and particle-substrate interactions.

Starting from an in-depth understanding of yet-known mechanochemical activation by ball milling, we demonstrated that wet comminution by stirred media milling is a versatile and scalable strategy for the fabrication of binder-free anodes in alkaline water electrolysis. By circumventing the need for polymeric binders, this approach overcomes key limitations related to ink formulation, binder-induced conductivity loss, and mechanical delamination. The process further enables direct catalyst deposition from in situ-prepared inks, opening new opportunities for integrating active materials into advanced electrode architectures. We believe that stirred media milling holds substantial promise for the scalable preparation of active, binder-free anodes for AWE, and is potentially transferable to other electrochemical applications, including anion exchange membrane (AEM) electrolysis, where similar requirements for high surface hydroxylation, enhanced adhesion, and mechanical robustness exist.

Acknowledgements

The authors acknowledge financial support from the German Federal Ministry of Research, Technology and Space (BMFTR project “PrometH2eus”, FKZ XXX). We extend our thanks to M. Heidelmann and U. Hagemann from the Interdisciplinary Center for Analytics on the Nanoscale (ICAN) for their valuable assistance with TEM and XPS measurements. Beate Endres was acknowledged for her help with the N_2 sorption measurements. V.V. thank university of Duisburg-Essen for Postdoc Seed Funding and Open Access funding enabled and organized by Projekt DEAL. J.J. acknowledge financial support from Max Planck Society and Deutsche Forschungsgemeinschaft (DFG, German Research Foundation), under Germany's Excellence Strategy – Exzellenzcluster 2186 “The Fuel Science Center,” no. 390919832. J.J. and M.F.T. thank John-Tommes Krzeslack for the support with XPS measurements.

References

1 Z. Abdin, A. Zafaranloo, A. Rafiee, W. Mérida, W. Lipiński and K. R. Khalilpour, Hydrogen as an energy vector, *Renewable and Sustainable Energy Reviews*, 2020, **120**, 109620.
2 Y. Yuan, H. Fang, K. Chen, J. Huang, J. Chen, Z. Lu, H. Wang, Z. Zhao, W. Chen and Z. Wen, Engineering High-Density Grain Boundaries in Ru0.8Ir0.2Ox Solid-Solution Nanosheets for Efficient and Durable OER Electrocatalysis, *Advanced Materials*, 2025, **37**, e2501607.
3 D. Strmcnik, P. P. Lopes, B. Genorio, V. R. Stamenkovic and N. M. Markovic, Design principles for hydrogen evolution reaction catalyst materials, *Nano Energy*, 2016, **29**, 29–36.
4 N. Johnson, M. Liebreich, D. M. Kammen, P. Ekins, R. McKenna and I. Staffell, Realistic roles for hydrogen in the future energy transition, *Nat. Rev. Clean Technol.*, 2025, **1**, 351–371.
5 T. Audichon, T. W. Napporn, C. Canaff, C. Morais, C. Comminges and K. B. Kokoh, IrO 2 Coated on RuO 2 as Efficient and Stable Electroactive Nanocatalysts for Electrochemical Water Splitting, *J. Phys. Chem. C*, 2016, **120**, 2562–2573.
6 M. Chen, S. X. Tan, S. Cheng, Y.-Y. Chen, Y.-H. Hsu, S.-F. Hung, L. Zhang and J. Gao, Revisiting the ruthenium oxide-based water oxidation catalysts in acidic media: From amorphous to crystalline, *Nano Energy*, 2025, **137**, 110800.
7 S. Chu, Y. Cui and N. Liu, The path towards sustainable energy, *Nature Mater*, 2016, **16**, 16–22.
8 T. Tran-Phu, R. Daiyan, J. Leverett, Z. Fusco, A. Tadich, I. Di Bernardo, A. Kiy, T. N. Truong, Q. Zhang, H. Chen, P. Kluth, R. Amal and A. Tricoli, Understanding the activity and stability of flame-made Co3O4 spinels: A route towards the scalable production of highly performing OER electrocatalysts, *Chemical Engineering Journal*, 2022, **429**, 132180.
9 K. Wang, X. Wang, Z. Li, B. Yang, M. Ling, X. Gao, J. Lu, Q. Shi, L. Lei, G. Wu and Y. Hou, Designing 3d dual transition metal electrocatalysts for oxygen evolution reaction in alkaline electrolyte: Beyond oxides, *Nano Energy*, 2020, **77**, 105162.
10 L. Magnier, G. Cossard, V. Martin, C. Pascal, V. Roche, E. Sibert, I. Shchedrina, R. Bousquet, V. Parry and M. Chatenet, Fe-Ni-based alloys as highly active and low-cost oxygen evolution reaction catalyst in alkaline media, *Nat. Mater.*, 2024, **23**, 252–261.
11 J. Yu, Y. Zhong, W. Zhou and Z. Shao, Facile synthesis of nitrogen-doped carbon nanotubes encapsulating nickel cobalt alloys 3D networks for oxygen evolution reaction in an alkaline solution, *Journal of Power Sources*, 2017, **338**, 26–33.

12 J. Qi, W. Zhang, R. Xiang, K. Liu, H.-Y. Wang, M. Chen, Y. Han and R. Cao, Porous Nickel-Iron Oxide as a Highly Efficient Electrocatalyst for Oxygen Evolution Reaction, *Advanced science (Weinheim, Baden-Wurttemberg, Germany)*, 2015, **2**, 1500199.
13 T. Zhou, Z. Cao, P. Zhang, H. Ma, Z. Gao, H. Wang, Y. Lu, J. He and Y. Zhao, Transition metal ions regulated oxygen evolution reaction performance of Ni-based hydroxides hierarchical nanoarrays, *Sci Rep*, 2017, **7**, 46154.
14 H. Wan, F. Chen, W. Ma, X. Liu and R. Ma, Advanced electrocatalysts based on two-dimensional transition metal hydroxides and their composites for alkaline oxygen reduction reaction, *Nanoscale*, 2020, **12**, 21479–21496.
15 Y. Du, S. Khan, X. Zhang, G. Yu, R. Liu, B. Zheng, R. Nadimicherla, D. Wu and R. Fu, In-situ preparation of porous carbon nanosheets loaded with metal chalcogenides for a superior oxygen evolution reaction, *Carbon*, 2019, **149**, 144–151.
16 M. Braun, M. Chatwani, P. Kumar, Y. Hao, I. Sanjuán, A.-A. Apostoleri, A. C. Brix, D. M. Morales, U. Hagemann, M. Heidelmann, J. Masa, W. Schuhmann and C. Andronescu, Cobalt nickel boride as electrocatalyst for the oxidation of alcohols in alkaline media, *J. Phys. Energy*, 2023, **5**, 24005.
17 Z.-P. Wu, X. F. Lu, S.-Q. Zang and X. W. Lou, Non-Noble-Metal-Based Electrocatalysts toward the Oxygen Evolution Reaction, *Advanced Functional Materials*, 2020, **30**, 1910274.
18 A. M. Alharthi, O. A. Hazazi, B. A. Al Jahdaly, M. A. Kassem and M. I. Awad, Boosting the Electrochemical Oxygen Evolution with Nickel Oxide Nanoparticle-Modified Glassy Carbon Electrodes in Alkaline Solutions, *ACS Omega*, 2024. DOI: 10.1021/acsomega.4c04700.
19 A. Singh, S. L. Y. Chang, R. K. Hocking, U. Bach and L. Spiccia, Highly active nickel oxide water oxidation catalysts deposited from molecular complexes, *Energy Environ. Sci.*, 2013, **6**, 579–586.
20 C. Gao, Y. Zhang, S. Mia, T. Xing and G. Chen, Development of inkjet printing ink based on component solubility parameters and its properties, *Colloids and Surfaces A: Physicochemical and Engineering Aspects*, 2021, **609**, 125676.
21 C. A. Charitidis, P. Georgiou, M. A. Koklioti, A.-F. Trompeta and V. Markakis, Manufacturing nanomaterials: from research to industry, *Manufacturing Rev.*, 2014, **1**, 11.
22 D. Yang, Y. Guo, H. Tang, Y. Wang, D. Yang, P. Ming, C. Zhang, B. Li and S. Zhu, Influence of the dispersion state of ionomer on the dispersion of catalyst ink and the construction of catalyst layer, *International Journal of Hydrogen Energy*, 2021, **46**, 33300–33313.
23 S. Chandrasekaran, M. Khandelwal, F. Dayong, L. Sui, J. S. Chung, R. D. K. Misra, P. Yin, E. J. Kim, W. Kim, A. Vanchiappan, Y. Liu, S. H. Hur, H. Zhang and C. Bowen, Developments and Perspectives on Robust Nano- and Microstructured Binder-Free Electrodes for Bifunctional Water Electrolysis and Beyond, *Advanced Energy Materials*, 2022, **12**. DOI: 10.1002/aenm.202200409.
24 J. Qian, C. Wang, X. Zhang, J. Hu, X. Zhao, J. Li and Q. Ren, Quaternary ammonium-functionalized crosslinked poly(aryl ether sulfone)s anion exchange membranes with enhanced alkaline stability for water electrolysis, *Journal of Membrane Science*, 2023, **685**, 121946.
25 R. A. Krivina, G. A. Lindquist, S. R. Beaudoin, T. N. Stovall, W. L. Thompson, L. P. Twight, D. Marsh, J. Grzyb, K. Fabrizio, J. E. Hutchison and S. W. Boettcher, Anode Catalysts in Anion-Exchange-Membrane Electrolysis without Supporting Electrolyte: Conductivity, Dynamics, and Ionomer Degradation, *Advanced Materials*, 2022, **34**, e2203033.
26 S. S. Koshy, J. Rath and A. Kiani, Fabrication of binder-less metal electrodes for electrochemical water splitting - A review, *Heliyon*, 2024, **10**, e37188.
27 *Enhanced water oxidation reaction by binder-free nickel oxide nanorod arrays electrocatalyst*, 2024.

28 S. Bhandari, R. Schierholz, R.-A. Eichel, A. L. Luna and A. K. Mechler, Exploring the Effect of Ball Milling on the Physicochemical Properties and Oxygen Evolution Reaction Activity of Nickel and Cobalt Oxides, *Adv Energy and Sustain Res*, 2024. DOI: 10.1002/aesr.202400183.
29 H. Kahimbi, S. B. Hong, M. Yang and B. G. Choi, Simultaneous synthesis of NiO/reduced graphene oxide composites by ball milling using bulk Ni and graphite oxide for supercapacitor applications, *Journal of Electroanalytical Chemistry*, 2017, **786**, 14–19.
30 C. F. Burmeister and A. Kwade, Process engineering with planetary ball mills, *Chemical Society Reviews*, 2013, **42**, 7660–7667.
31 A. S. Amin, D. Lerche, A. S. Odungat, S. U. Boehm, T. Koch, F. Özcan and D. Segets, A Procedure for Rational Probe Liquids Selection to Determine Hansen Solubility Parameters, *ChemCatChem*, 2024, **16**. DOI: 10.1002/cctc.202301393.
32 S. Bapat and D. Segets, Sedimentation Dynamics of Colloidal Formulations through Direct Visualization: Implications for Fuel Cell Catalyst Inks, *ACS Appl. Nano Mater.*, 2020, **3**, 7384–7391.
33 A. Jain, V. Vinayakumar, A. Olean-Oliveira, C. Marcks, M. Chatwani, A. K. Mechler, C. Andronescu and D. Segets, From Small-Area Observations to Insight: Surface-Feature-Extrapolation of Anodes for Alkaline Oxygen Evolution Reaction, *ChemCatChem*, 2024, **16**. DOI: 10.1002/cctc.202301461.
34 S. Brunauer, P. H. Emmett and E. Teller, Adsorption of Gases in Multimolecular Layers, *J. Am. Chem. Soc.*, 1938, **60**, 309–319.
35 F. T. L. Muniz, M. A. R. Miranda, C. Morilla dos Santos and J. M. Sasaki, The Scherrer equation and the dynamical theory of X-ray diffraction, *Acta Crystallogr A Found Adv*, 2016, **72**, 385–390.
36 C. J. Humphreys, The significance of Bragg's law in electron diffraction and microscopy, and Bragg's second law, *Acta crystallographica. Section A, Foundations of crystallography*, 2013, **69**, 45–50.
37 S. C. Chopade, I. G. Kore, S. P. Patil, N. D. Jadhav, C. Srinidhi and P. A. Desai, Lattice geometry controlled synthesis of Cu – Doped nickel oxide nanoparticles, *Ceramics International*, 2018, **44**, 5621–5628.
38 B. Himabindu, N. Latha Devi and B. Rajini Kanth, Microstructural parameters from X-ray peak profile analysis by Williamson-Hall models; A review, *Materials Today: Proceedings*, 2021, **47**, 4891–4896.
39 S. Süß, T. Sobisch, W. Peukert, D. Lerche and D. Segets, Determination of Hansen parameters for particles: A standardized routine based on analytical centrifugation, *Advanced Powder Technology*, 2018, **29**, 1550–1561.
40 S. Bapat, S. O. Kilian, H. Wiggers and D. Segets, Towards a framework for evaluating and reporting Hansen solubility parameters: applications to particle dispersions, *Nanoscale advances*, 2021, **3**, 4400–4410.
41 A. Sze, D. Erickson, L. Ren and D. Li, Zeta-potential measurement using the Smoluchowski equation and the slope of the current-time relationship in electroosmotic flow, *Journal of Colloid and Interface Science*, 2003, **261**, 402–410.
42 N. Thissen, J. Hoffmann, S. Tigges, D. A. M. Vogel, J. J. Thoede, S. Khan, N. Schmitt, S. Heumann, B. J. M. Etzold and A. K. Mechler, Industrially Relevant Conditions in Lab-Scale Analysis for Alkaline Water Electrolysis, *ChemElectroChem*, 2024, **11**, e202300432.
43 G. Jerkiewicz, Standard and Reversible Hydrogen Electrodes: Theory, Design, Operation, and Applications, *ACS Catal.*, 2020, **10**, 8409–8417.
44 N. Mironova-Ulmane, A. Kuzmin, I. Sildos, L. Puust and J. Grabis, Magnon and Phonon Excitations in Nanosized NiO, *Latvian Journal of Physics and Technical Sciences*, 2019, **56**, 61–72.

45 P.A. Sheena, EFFECT OF CALCINATION TEMPERATURE ON THE STRUCTURAL AND OPTICAL PROPERTIES OF NICKEL OXIDE NANOPARTICLES, 2014, **5 (3)**, 441–449.
46 M. P. Deshpande, K. N. Patel, V. P. Gujarati, K. Patel and S. H. Chaki, Structural, Thermal and Optical Properties of Nickel Oxide (NiO) Nanoparticles Synthesized by Chemical Precipitation Method, *AMR*, 2016, **1141**, 65–71.
47 M. Kruk and M. Jaroniec, Gas Adsorption Characterization of Ordered Organic−Inorganic Nanocomposite Materials, *Chem. Mater.*, 2001, **13**, 3169–3183.
48 F. Fazlali, A. r. Mahjoub and R. Abazari, A new route for synthesis of spherical NiO nanoparticles via emulsion nano-reactors with enhanced photocatalytic activity, *Solid State Sciences*, 2015, **48**, 263–269.
49 Y. Lu, A. Frano, M. Bluschke, M. Hepting, S. Macke, J. Strempfer, P. Wochner, G. Cristiani, G. Logvenov, H.-U. Habermeier, M. W. Haverkort, B. Keimer and E. Benckiser, Quantitative determination of bond order and lattice distortions in nickel oxide heterostructures by resonant x-ray scattering, *Phys. Rev. B*, 2016, **93**. DOI: 10.1103/physrevb.93.165121.
50 N. Mironova-Ulmane, A. Kuzmin, J. Grabis, I. Sildos, V. I. Voronin, I. F. Berger and V. A. Kazantsev, Structural and Magnetic Properties of Nickel Oxide Nanopowders, *SSP*, 2010, **168-169**, 341–344.
51 N. Bala, H. K. Singh, S. Verma and S. Rath, Magnetic-order induced effects in nanocrystalline NiO probed by Raman spectroscopy, *Phys. Rev. B*, 2020, **102**. DOI: 10.1103/PhysRevB.102.024423.
52 J. Dong, Z. Qian, P. Xu, M.-F. Yue, R.-Y. Zhou, Y. Wang, Z.-A. Nan, S. Huang, Q. Dong, J.-F. Li, F. R. Fan and Z.-Q. Tian, In situ Raman spectroscopy reveals the structure evolution and lattice oxygen reaction pathway induced by the crystalline-amorphous heterojunction for water oxidation, *Chemical Science*, 2022, **13**, 5639–5649.
53 H. Mio, J. Kano, F. Saito and K. Kaneko, Optimum revolution and rotational directions and their speeds in planetary ball milling, *International Journal of Mineral Processing*, 2004, **74**, S85-S92.
54 *An overview of high-energy ball milled nanocrystalline aluminum alloys*, 2017.
55 W. Peukert, H.-C. Schwarzer, M. Götzinger, L. Günther and F. Stenger, Control of particle interfaces — the critical issue in nanoparticle technology, *Advanced Powder Technology*, 2003, **14**, 411–426.
56 *Polymorphic transformation and powder characteristics of TiO2 during high energy milling*, 2000.
57 Q. S. SONG, C. H. CHIU and S. CHAN, Effects of ball milling on the physical and electrochemical characteristics of nickel hydroxide powder, *J Appl Electrochem*, 2006, **36**, 97–103.
58 P. Ravikumar, B. Kisan and A. Perumal, Enhanced room temperature ferromagnetism in antiferromagnetic NiO nanoparticles, *AIP Advances*, 2015, **5**. DOI: 10.1063/1.4928426.
59 G. Anandha Babu, G. Ravi, M. Navaneethan, M. Arivanandhan and Y. Hayakawa, An investigation of flower shaped NiO nanostructures by microwave and hydrothermal route, *J Mater Sci: Mater Electron*, 2014, **25**, 5231–5240.
60 P. Hermet, L. Gourrier, J.-L. Bantignies, D. Ravot, T. Michel, S. Deabate, P. Boulet and F. Henn, Dielectric, magnetic, and phonon properties of nickel hydroxide, *Phys. Rev. B*, 2011, **84**. DOI: 10.1103/physrevb.84.235211.
61 P. T. Babar, A. C. Lokhande, M. G. Gang, B. S. Pawar, S. M. Pawar and J. H. Kim, Thermally oxidized porous NiO as an efficient oxygen evolution reaction (OER) electrocatalyst for electrochemical water splitting application, *Journal of Industrial and Engineering Chemistry*, 2018, **60**, 493–497.

62 J. Kwon, H. Han, S. Jo, S. Choi, K. Y. Chung, G. Ali, K. Park, U. Paik and T. Song, Amorphous Nickel–Iron Borophosphate for a Robust and Efficient Oxygen Evolution Reaction, *Advanced Energy Materials*, 2021, **11**. DOI: 10.1002/aenm.202100624.
63 H. Radinger, P. Connor, S. Tengeler, R. W. Stark, W. Jaegermann and B. Kaiser, Importance of Nickel Oxide Lattice Defects for Efficient Oxygen Evolution Reaction, *Chem. Mater.*, 2021, **33**, 8259–8266.
64 M. Hammad, S. Angel, A. K. Al-Kamal, A. Asghar, A. Said Amin, M.-A. Kräenbring, H. T. Wiedemann, V. Vinayakumar, M. Yusuf Ali, P. Fortugno, C. Kim, T. C. Schmidt, C. W. Kay, C. Schulz, D. Segets and H. Wiggers, Synthesis of novel LaCoO3/graphene catalysts as highly efficient peroxymonosulfate activator for the degradation of organic pollutants, *Chemical Engineering Journal*, 2023, **454**, 139900.
65 M. Cui, X. Ding, X. Huang, Z. Shen, T.-L. Lee, F. E. Oropeza, J. P. Hofmann, E. J. M. Hensen and K. H. L. Zhang, Ni 3+ -Induced Hole States Enhance the Oxygen Evolution Reaction Activity of Ni x Co 3– x O 4 Electrocatalysts, *Chem. Mater.*, 2019, **31**, 7618–7625.
66 H. P. Tran, H. N. Nong, H.-S. Oh, M. Klingenhof, M. Kroschel, B. Paul, J. Hübner, D. Teschner and P. Strasser, Catalyst–Support Surface Charge Effects on Structure and Activity of IrNi-Based Oxygen Evolution Reaction Catalysts Deposited on Tin-Oxide Supports, *Chem. Mater.*, 2022, **34**, 9350–9363.
67 *The relationship between pH and zeta potential of ∼30 nm metal oxide nanoparticle suspensions relevant to in vitro toxicological evaluations*, 2009.
68 X. Zhao, W. Liu, Z. Cai, B. Han, T. Qian and D. Zhao, An overview of preparation and applications of stabilized zero-valent iron nanoparticles for soil and groundwater remediation, *Water Research*, 2016, **100**, 245–266.
69 A. Alfarra, E. Frackowiak and F. Béguin, The HSAB concept as a means to interpret the adsorption of metal ions onto activated carbons, *Applied Surface Science*, 2004, **228**, 84–92.
70 R. K. Dwari and B. K. Mishra, Evaluation of flocculation characteristics of kaolinite dispersion system using guar gum: A green flocculant, *International Journal of Mining Science and Technology*, 2019, **29**, 745–755.
71 A. Jain, C. Marcks, L. Grebener, J. Johny, A. S. Odungat, M. Chatwani, M.-A. Kräenbring, A. Shaji, M. F. Tesch, A. K. Mechler, V. Vinayakumar and D. Segets, A Proof-of-Principle Demonstration: Exploring the Effect of Anode Layer Microstructure on the Alkaline Oxygen Evolution Reaction, *Advanced Functional Materials*, 2025, 2421352.
72 R. S. Hebbar, A. M. Isloor and A. F. Ismail, Contact Angle Measurements, *Membrane Characterization*, 2017, 219–255.
73 S. G. Randive and B. J. Lokhande, Spray pyrolyzed hydrophilic nickel oxide electrodes with nano-granular morphology for a symmetric supercapacitor device, *Journal of Alloys and Compounds*, 2023, **944**, 169046.
74 T. L. Liu, Z. Chen and C.-J. Kim, A dynamic Cassie-Baxter model, *Soft Matter*, 2015, **11**, 1589–1596.
75 F. Tang, W. Cheng, Y. Huang, H. Su, T. Yao, Q. Liu, J. Liu, F. Hu, Y. Jiang, Z. Sun and S. Wei, Strong Surface Hydrophilicity in Co-Based Electrocatalysts for Water Oxidation, *ACS applied materials & interfaces*, 2017, **9**, 26867–26873.
76 Z. Xiao, H. Wang, N. Cai, Y. Li, K. Xiang, W. Wei, T. Ye, Z. Zhang, S. Wang and Z. Tang, Enhancement of –OH content on mechanical properties of antiperovskite solid electrolytes, *Nano Res.*, 2024, **17**, 6139–6146.
77 *Design of an alkaline water electrolyzer for hydrogen production*, 2023.
78 A. Kwade, A Stressing Model for the Description and Optimization of Grinding Processes, *Chemical Engineering & Technology*, 2003, **26**, 199–205.

79 D. Siegmund, S. Metz, V. Peinecke, T. E. Warner, C. Cremers, A. Grevé, T. Smolinka, D. Segets and U.-P. Apfel, Crossing the Valley of Death: From Fundamental to Applied Research in Electrolysis, *JACS Au*, 2021, **1**, 527–535.
80 C. Gohlke, J. Gallenberger, N. Niederprüm, H. Ingendae, J. Kautz, J. P. Hofmann and A. K. Mechler, Boosting the Oxygen Evolution Reaction Performance of Ni-Fe-Electrodes by Tailored Conditioning, *ChemElectroChem*, 2024, **11**, e202400318.
81 X. Liu, Z. He, M. Ajmal, C. Shi, R. Gao, L. Pan, Z.-F. Huang, X. Zhang and J.-J. Zou, Recent Advances in the Comprehension and Regulation of Lattice Oxygen Oxidation Mechanism in Oxygen Evolution Reaction, *Trans. Tianjin Univ.*, 2023, **29**, 247–253.

Supplementary information

Mechanochemical activation of nickel oxide: a pivotal step in the process chain enabling binder-free-anodes for alkaline water electrolysis

Mohit Chatwani*, Adarsh Jain, Christian Marcks, Jacob Johny, Lars Grebener, Hao Yun, Ali Raza Khan, Georg Bendt, Stefan Romeis, Viktor Čolić, Marc Frederic Tesch, Anna K. Mechler, Vineetha Vinayakumar, Doris Segets*

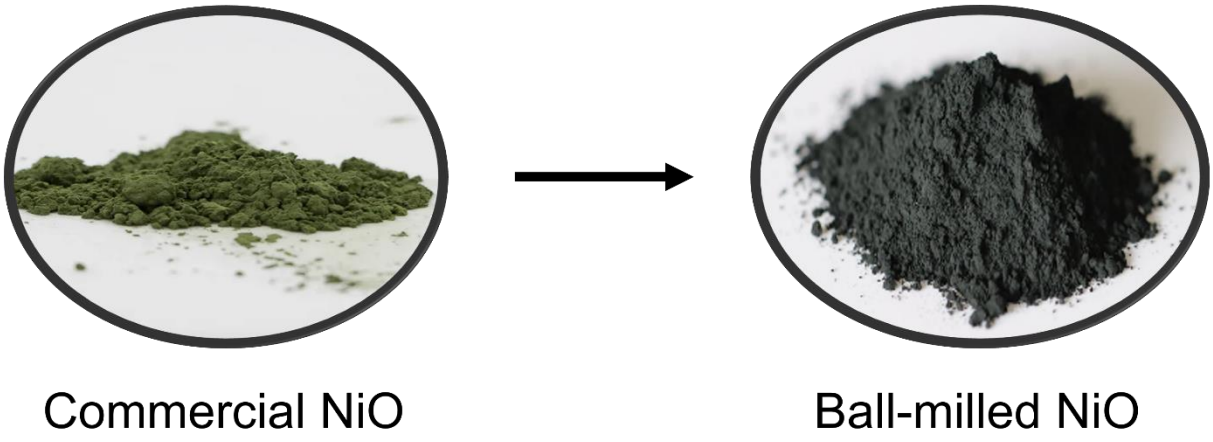

Figure S1 Green colored commercial NiO powder transformed to dark grey color after ball milling.

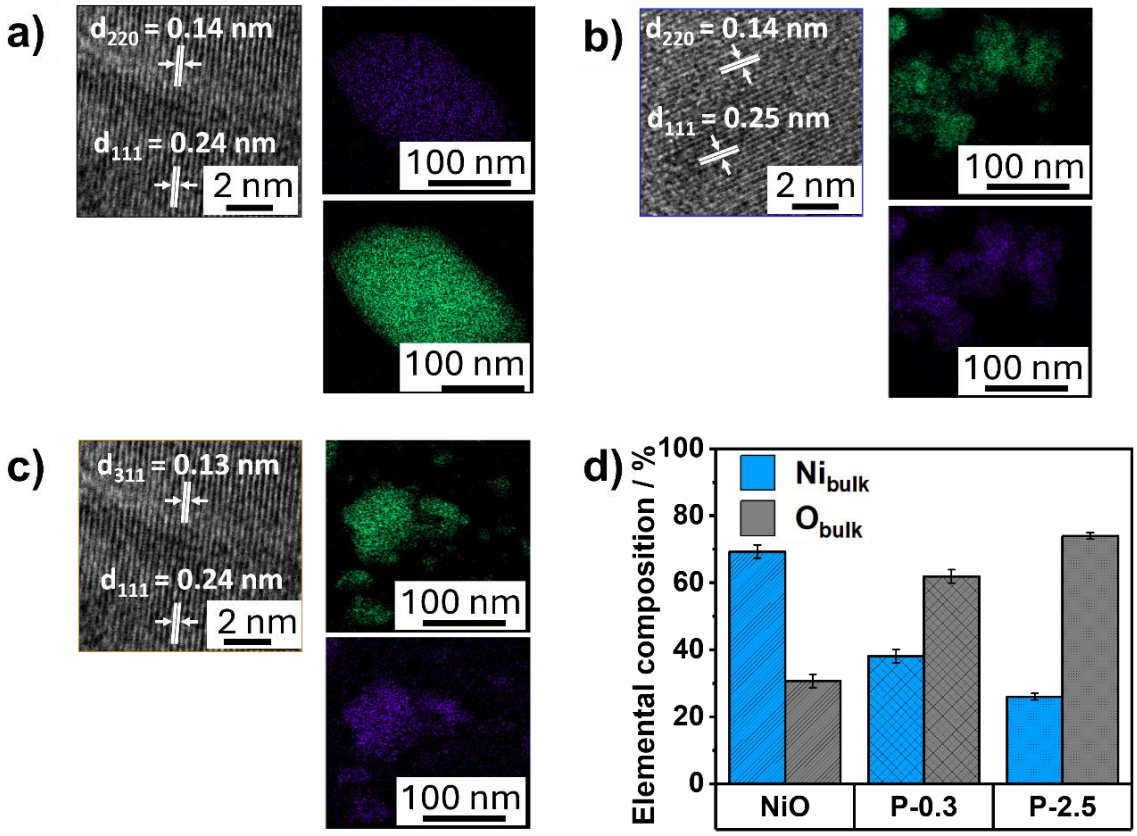

Figure S2 Interplanar spacing from TEM micrographs and EDX mappings for a) NiO b) P-0.3, and c) P-2.5.

The EDX mapping illustrated in Figure S2(a-c) shows the spatial distribution of Ni (green) and O (purple), for both pristine NiO and ball milled samples, evidencing a homogeneous distribution of Ni and O in all samples. The HRTEM (High-Resolution TEM) images shown in the insets of Figure S2 reveal distinct crystal lattice fringes with interplanar spacings of approximately 0.14 nm, 0.24 nm, and 0.13 nm, corresponding to the [220], [111], and [311] crystal planes of the NiO phase (JCPDS #22-1189). These observations confirm the polycrystalline nature of the materials.

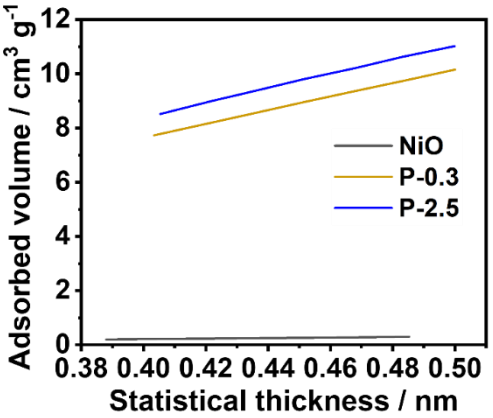

Figure S3 t-plot from N_2 sorption measurements of NiO, P-0.3, and P-2.5 powders.

Table S1 XPS fitted data values of $Ni2p_{3/2}$ deconvoluted spectra for NiO, P-0.3, and P-2.5.

Sample	Correlation coefficient	C constant
NiO	0.9990	19
P-0.3	0.9998	105
P-2.5	0.9999	83

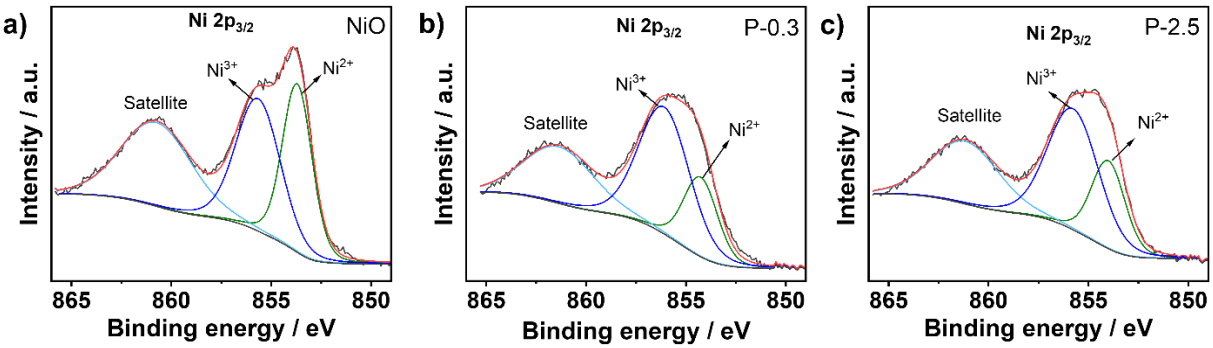

Figure S4 Deconvoluted XPS spectra showing $Ni2p_{3/2}$ regions of (a) NiO, (b) P-0.3, and (c) P-2.5.

In Figure S4a, the $Ni2p_{3/2}$ spectrum of pristine NiO and its ball milled derivatives was deconvoluted into three peaks with binding energy values located around 854.1, 855.3, and 861.4 eV where the peak at 861.4 is a satellite peak. The main Ni-$2p_{3/2}$ peaks located at 854.1 eV and 855.3 eV are assigned to Ni^{3+} and Ni^{2+} contributions, respectively.

Table S5 XPS fitted data values of $Ni2p_{3/2}$ deconvoluted spectra for NiO, P-0.3, and P-2.5.

NiO			P-0.3			P-2.5		
Position	**FWHM**	**% Area**	**Position**	**FWHM**	**% Area**	**Position**	**FWHM**	**% Area**
853.81	1.75	29.91	854.20	2.00	20.62	854.00	1.98	22.21
855.65	2.61	34.99	856.09	3.00	49.27	855.76	3.00	46.23
860.74	4.15	35.10	861.36	4.11	30.11	861.16	3.96	31.56

Table S3 XPS fitted data values of O1s deconvoluted spectra for NiO, P-0.3, and P-2.5.

NiO			P-0.3			P-2.5		
Position	**FWHM**	**% Area**	**Position**	**FWHM**	**% Area**	**Position**	**FWHM**	**% Area**
530.4	0.92	3.28	530.34	0.94	19.22	530.29	1.08	19.28
529.28-	1.42	70.10	529.38	1.40	29.90	529.30	1.40	41.77
531.24	1.70	26.62	531.42	1.60	40.55	531.36	1.60	35.15
			533.00	1.47	10.34	533.00	1.35	3.81

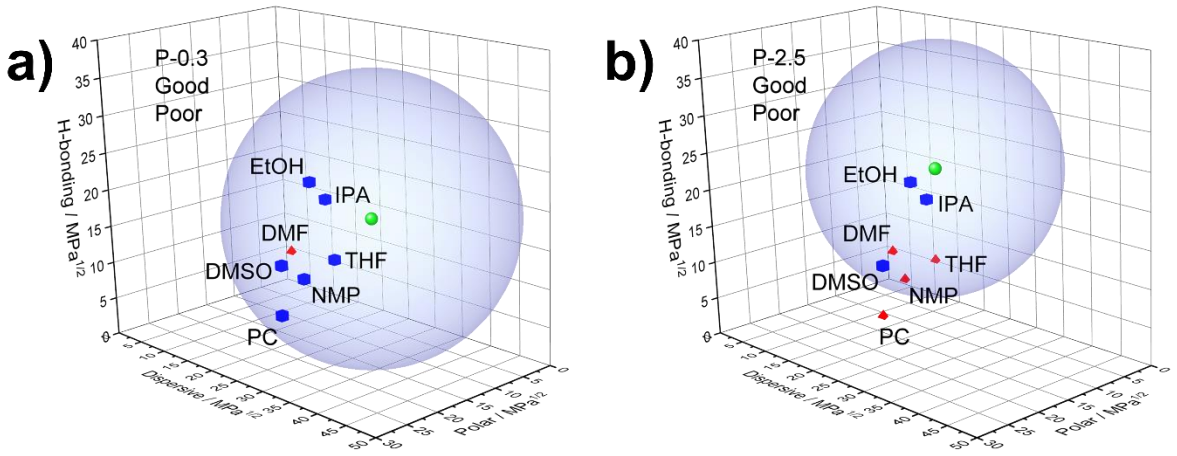

Figure S5 HSP sphere showing Dispersive (δD), Polar (δP) and H-bonding (δH) parameters for a) P-0.3 and b) P-2.5.

Table S4 Calculated δD, δP, and δH parameters from corresponding HSP spheres for samples P-0.3 and P-2.5.

Ball milled sample	δD ($MPa^{1/2}$)	δP ($MPa^{1/2}$)	δD ($MPa^{1/2}$)
P-0.3	25.48	6.76	15.79
P-2.5	23.12	10.87	22.99

The stability of each ink was further evaluated with S-scores as stability metric, also developed by us[32]. By examining the characteristic patterns observed during the sedimentation process, the initial ink stability and long-term susceptibility to settling were assessed as will be described in the following. As shown in Figure S6-a, pristine NiO sedimented almost instantly, confirming its high instability in ink formulations. Its large particle size and poor interactions with the solvent caused rapid settling within seconds, making it unsuitable for applications requiring long-term dispersion stability.

The S-scores determined from sedimentation times (Figure S6-b) further quantify these differences. The S-score profile for P-0.3 displayed a uniform settling pattern, with discrete fractions settling over short intervals, and maximum sedimentation occurring at ~18.5 min. In contrast, P-2.5 exhibited stepwise sedimentation, where the majority of particles settled after ~42 min, aligning with the observed size-dependent settling behavior.

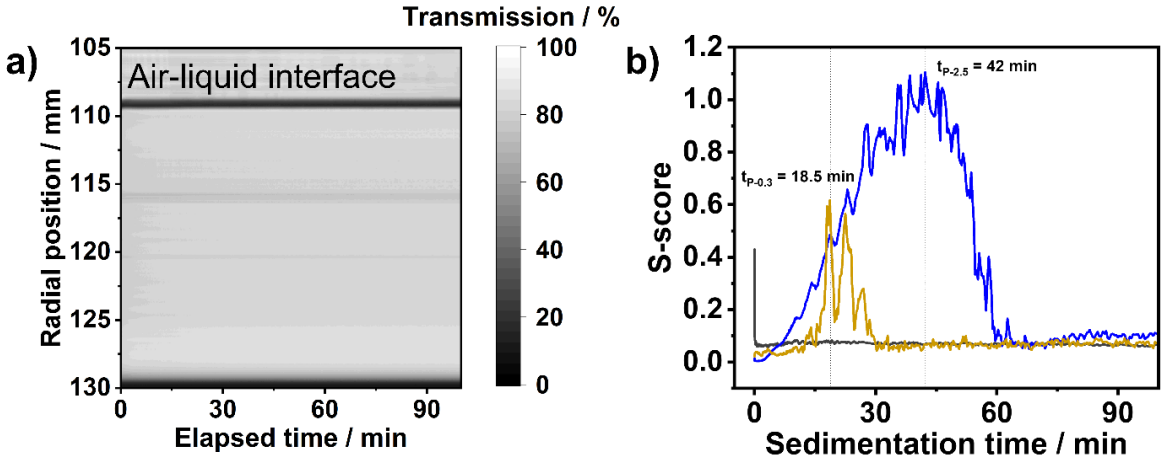

Figure S6 a) Transmittogram of pristine NiO dispersed in isopropanol having concentration of 1 mg mL-1. B) S-scores for NiO(grey), P-0.3 (dark yellow), and P-2.5 (blue) inks dispersed in isopropanol.

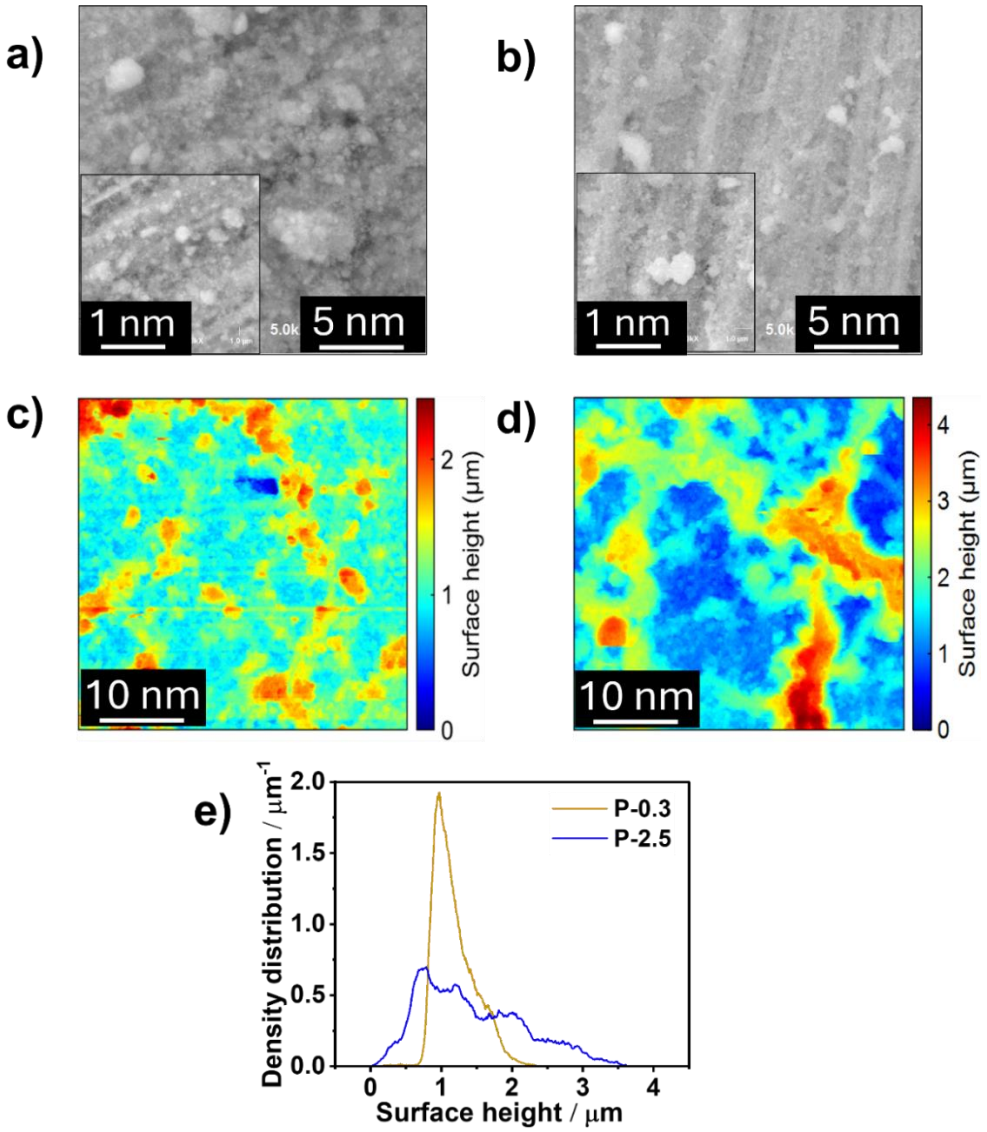

Figure S7 SEM images of spray coated anodes based on a) P-0.3 and b) P-2.5 particles on Ni plate substrate. AFM images of spray coated anodes based on c) P-0.3 and d) P-2.5 particles on Ni plate substrate. e) Density distribution of spray coated samples P-0.3 and P-2.5 derived from AFM image analysis.

Figure S7 presents the morphological characterization of anodes fabricated using P-0.3 and P-2.5 (refer to the Experimental Section for more details), examined through SEM and AFM. The SEM images in Figure S7a-b reveal distinct differences between P-0.3 and P-2.5. P-0.3 displays a non-uniform particle distribution, with larger agglomerates clearly visible in the inset magnification. The surface appears less dense and more granular. In contrast, P-2.5 exhibiting closely packed particles forming a compact and uniform surface texture. The magnified inset further highlights this dense arrangement, indicating higher agglomeration in P-0.3.

The AFM images in Figure S6c-d further support these observations. In P-0.3, the particles are uniformly distributed with lower surface height variations, contributing to a smoother, more consistent coating. In contrast, P-2.5 exhibits regions of elevated surface height, with larger agglomerates highlighted in red, reinforcing the SEM findings of non-uniformity and rougher surface texture. The quantitative AFM analysis in Figure S6e reveals that P-0.3 has a major height distribution centered at ~1 µm, with a narrow spread up to 2.3 µm, indicating a more compact and controlled surface structure. Conversely, P-2.5 exhibits a broader surface height distribution, with a major peak at 0.9 µm and heights reaching up to 4 µm, reflecting a higher degree of surface roughness and agglomeration. As the spray coating parameters and the continuous phase were kept constant, we mainly attribute these differences in surface morphology to slight differences in the agglomeration state of samples and, more pronounced, to changes in the drying dynamics. These are caused by the variation in the particles' surface properties that testament in the already observed particle-solvent-interaction and that are also expected to affect the interaction between particle and substrate. As demonstrated in our previous work[71], these morphological variations significantly impact key properties such as wettability and adhesion, which are crucial for electrochemical activity and stability.

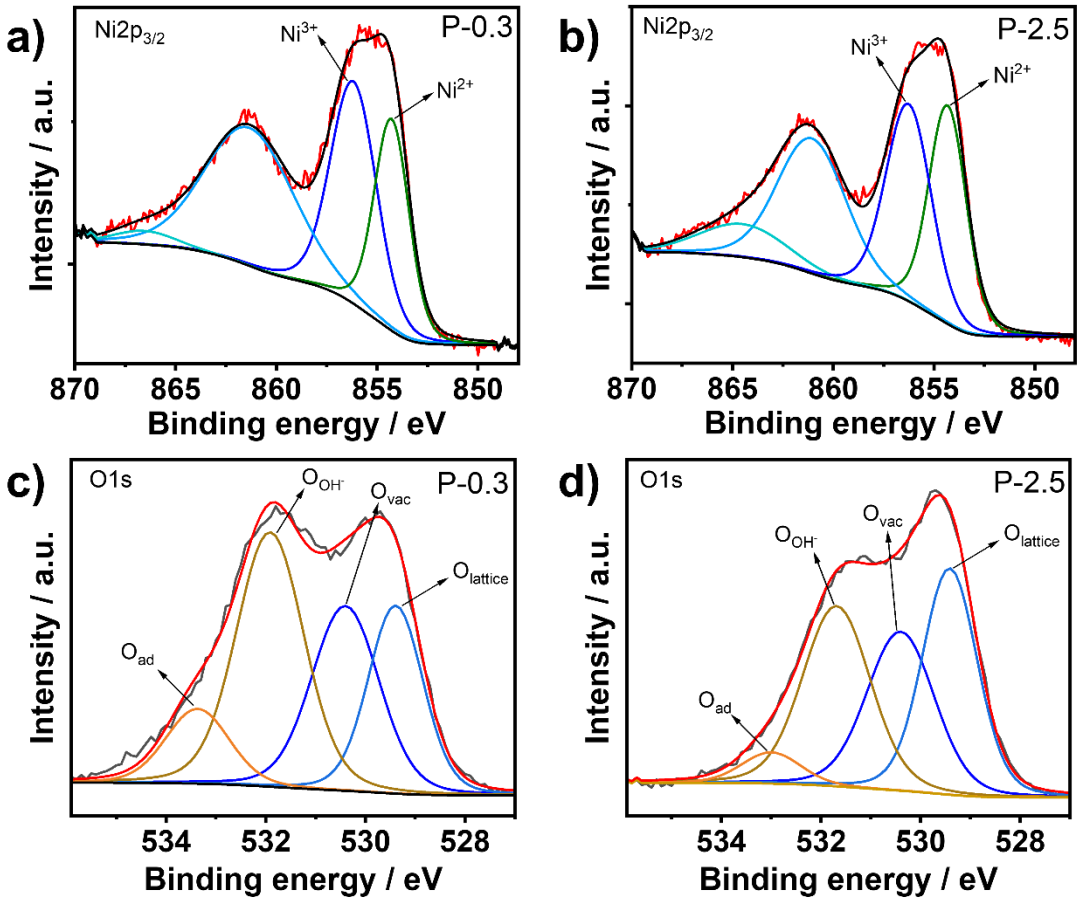

Figure S8 XPS deconvoluted spectra showing Ni2p$_{3/2}$ region for spray coated sample a) P-0.3, and b) P-2.5. XPS deconvoluted spectra of the O1s region for spray-coated samples: (c) P-0.3 and (d) P-2.5, highlighting distinct surface chemical states.

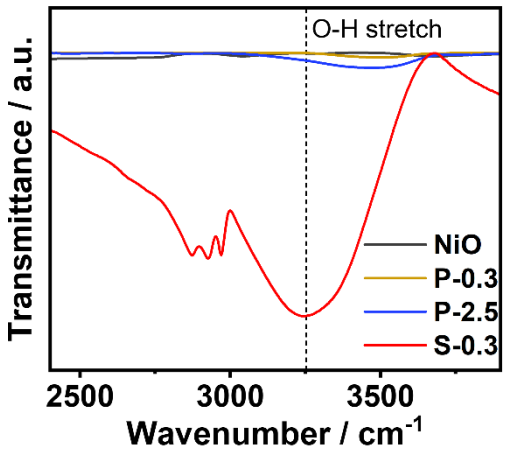

Figure S9 Fourier transform infrared spectra (FTIR) of NiO, P-0.3, P-2.5, and S-0.3 recorded within the 2450–3950 cm^{-1} range, showcasing differences in OH$_{bulk}$ groups.

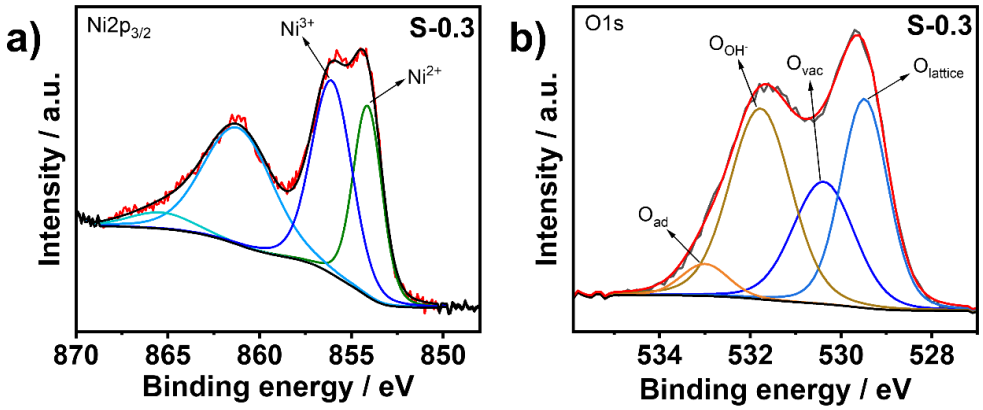

Figure S10 XPS deconvoluted spectra showing a) $Ni2p_{3/2}$ and b) O1s region for spray coated sample based on S-0.3 particles.

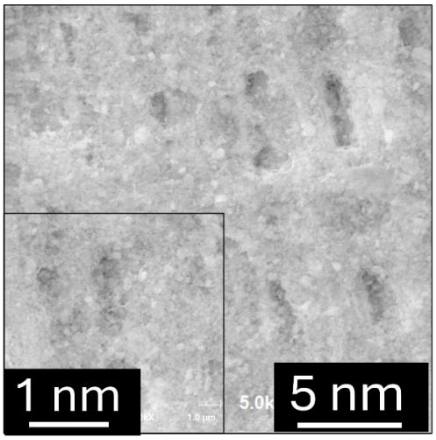

Figure S11 SEM images of spray coated anodes based on S-0.3 particles on Ni plate substrate.

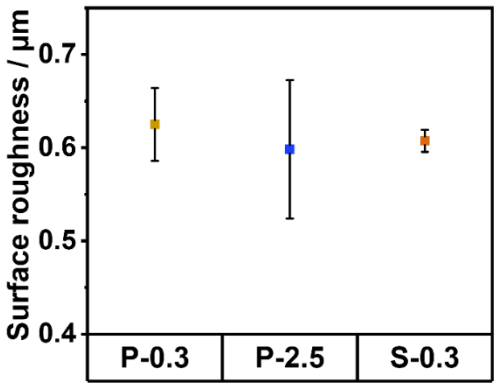

Figure S12 Root mean square surface roughness from 3D profilometry measurements for spray coated samples P-0.3, P-2.5, and S-0.3.

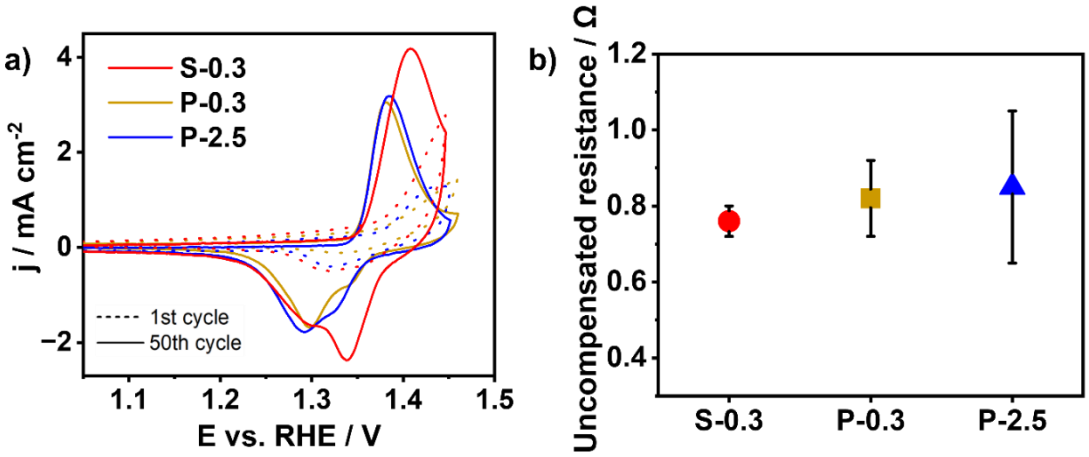

Figure S13 (a) Conditioning of S-0.3, P-2.5, and P-0.3 at potential window of 0.2-1.45 V vs. RHE with dashed lines showing 1st CV cycle and solid lines representing 50th CV cycle at 100 mV s^{-1}. (b) R_u between electrolyte, anode layer and support, measured at open circuit potential for S-0.3, P-2.5, and P-0.3 spray coated samples.

Post-mortem surface analysis

The post-OER XPS spectra of the Ni2$p_{3/2}$ and O1s regions, shown in Figure S14a-d, were recorded for both P-0.3 and P-2.5 coatings after the OER measurements to monitor potential changes in surface composition and stability.

The Ni2$p_{3/2}$ spectra reveal that the surface chemical states remain largely consistent with those observed prior to the OER process. Specifically, the characteristic peaks corresponding to Ni^{2+} and Ni^{3+} oxidation states are preserved in both samples, suggesting that the nickel species maintain their oxidation state distribution post-OER. Similarly, the O1s spectra exhibit features analogous to those of the pre-OER samples, indicating minimal surface reconstruction or compositional deviation. Both the samples retain its lattice oxygen and oxygen vacancies, ensuring chemical stability and long-term durability.

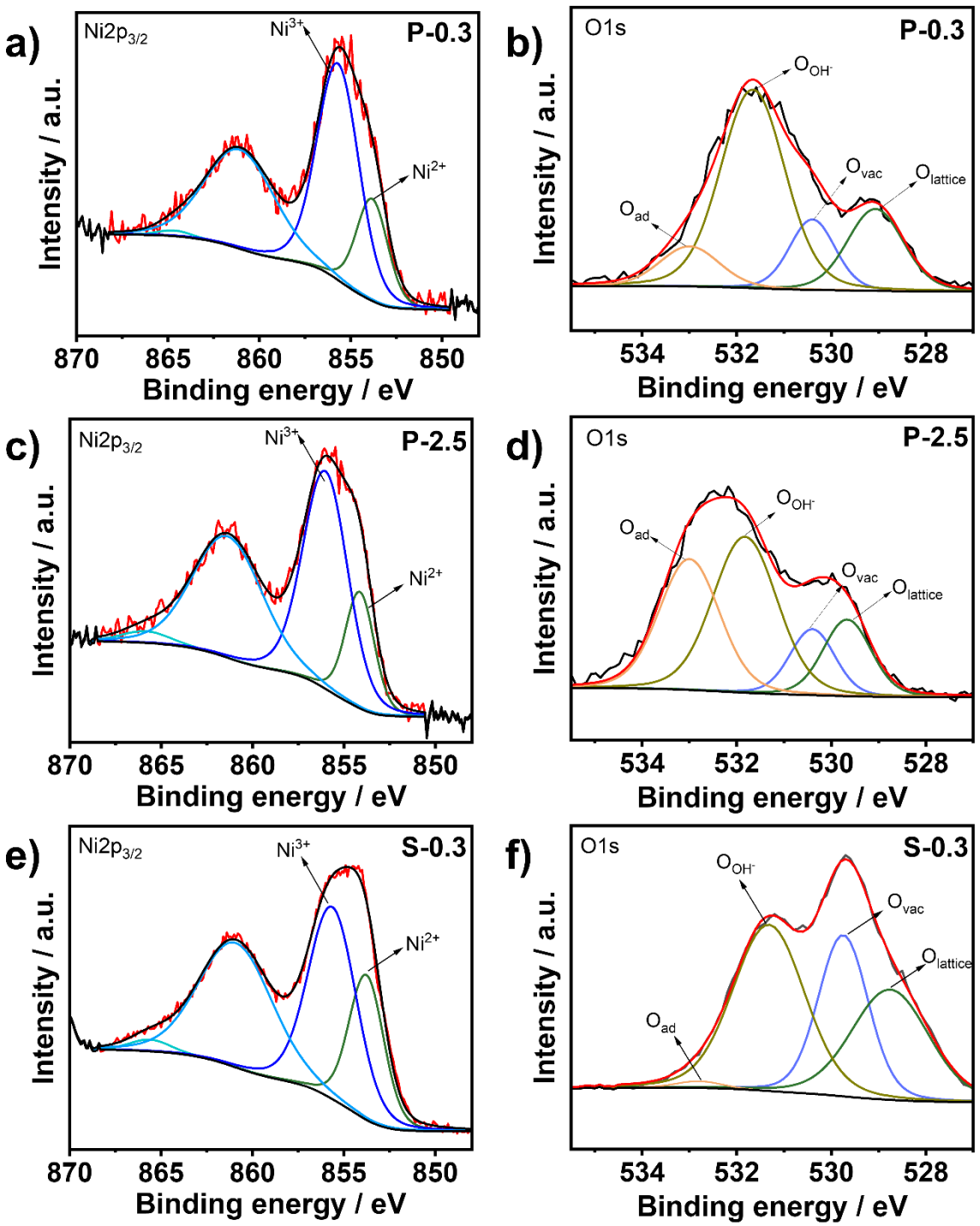

Figure S14 Deconvoluted XPS spectra of the $Ni2p_{3/2}$ region for spray-coated samples after electrochemical measurements: a) P-0.3, c) P-2.5, and e) S-0.3. Deconvoluted XPS spectra of the O1s region for the same samples: b) P-0.3, d) P-2.5, and f) S-0.3.

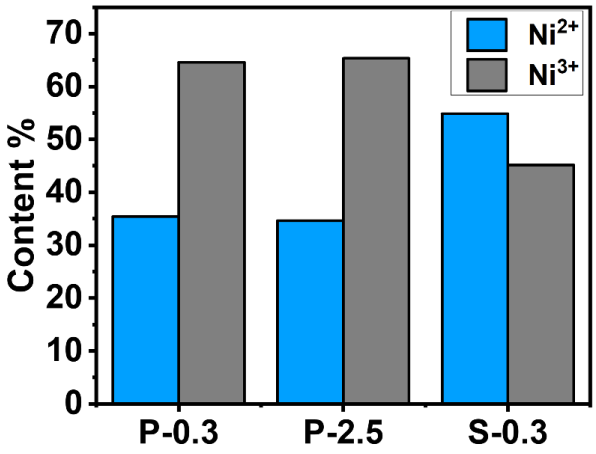

Figure S15 Ni^{2+} and Ni^{3+} contents derived from $Ni2p_{3/2}$ deconvoluted spectra for spray coated anodes based on a) P-0.3, b) P-2.5, and c) S-0.3 particles after beaker cell measurements.

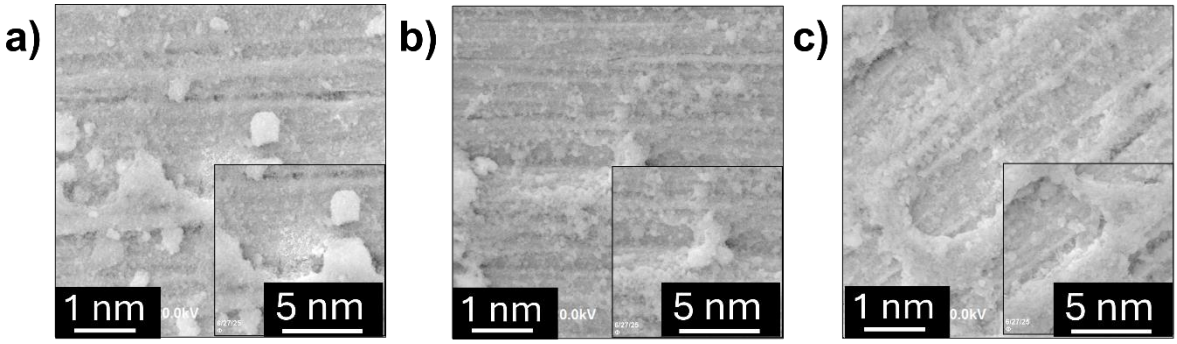

Figure S16 SEM images of spray coated anodes based on a) P-0.3, b) P-2.5, and c) S-0.3 particles after beaker cell measurements.